Inversion of transfer zones in salt-bearing extensional systems: insights from analogue modeling

Elizabeth P. Wilson, Pablo Granado, Pablo Santolaria, Oriol Ferrer, Josep Anton Muñoz

Institut de Recera Geomodels, Departament de Dinàmica de la Terra i de l'Oceà, Universitat de Barcelona, 08028, Barcelona, Spain

Correspondence to: Elizabeth P. Wilson (epwilson@ub.edu)

Abstract. This work uses sandbox analogue models to analyze the formation and subsequent inversion of a decoupled extensional system comprised of two segmented half-grabens with thick early syn-rift salt. The segmented half grabens strike perpendicular to the direction of extension and subsequent shortening. Rifting created first a basement topography that was

10   infilled by model salt, followed by a second phase of extension and sedimentation, followed afterwards by inversion. During the second phase of extension, syn-rift syncline minibasins developed above the basement extensional system and extended beyond the confines of the fault blocks. Sedimentary downbuilding and extension initiated the migration of model salt to the basement highs, forming salt anticlines, reactive diapirs, and salt walls perpendicular to the direction of extension, except for along the transfer zone where a slightly oblique salt anticline developed. Inversion resulted in decoupled cover and basement

15   thrust systems. Thrusts in the cover system nucleated along squeezed salt structures and along primary welds. New primary welds developed where the cover sequence touched down on basement thrust tips due to uplift, salt extrusion, and syn-contractional downbuilding caused by loading of syn-contractional sedimentation. Model geometries reveal the control imposed by the basement configuration and distribution of salt in the development of a thrust front from the inversion of a salt-bearing extensional system. In 3D, the interaction of salt migrating from adjacent syn-rift basins can modify the expected salt

20   structure geometry, which may in turn influence the location and style of thrust in the cover sequence upon inversion. Results are compared to the northern Lusitanian Basin, offshore Portugal and the Isàbena area of the South-Central Pyrenees, Spain.

1 Introduction

Salt tectonics plays a key role in the development of extensional basins, such as the Permian and Triassic basins in Northwestern Europe (e.g., Ziegler and van Hoorn, 1989; Stewart & Coward, 1995; Stewart, 2007; Soto et al., 2017; Ahlrichs

25   et al., 2020). Salt tectonics is also responsible for the characteristic structural styles of the circum-Mediterranean Alpine fold-and-thrust belts, such as the Ionian-Albanides (e.g. Velaj et al., 1999), the Tunisian Atlas (e.g. Saïd et al., 2011), the Swiss Helvetics (e.g. Sala et al. 2014) and Jura fold-and-thrust belt (Sommaruga, 1999), the southern Pyrenees (e.g. Muñoz et al., 2018), the Northern Calcareous Alps of Austria (e.g. Granado et al., 2019), or the SW France Sub-Alpine system (e.g. Célini et al., 2020). In salt-bearing extensional systems, the interaction between extensional basement faults and overlying salt layers

30   acts as the primary control on the structural evolution of the post-salt cover system (e.g., Vendeville and Jackson, 1992; Vendeville et al., 1995; Withjack et al., 1990; Koyi et al., 1993; Withjack and Callaway, 2000; Dooley et al., 2003, 2005; Richardson et al., 2005; Fig. 1). Upon thick-skinned extension, salt migrates towards the fault plane in the downthrown block below the cover sequence, forcing the syn-rift depocenters to develop away from the fault plane, while extensional forced folds develop above the footwall block (Vendeville and Jackson, 1995; Withjack and Callaway, 2000; Richardson et al. 2005; Ferrer

35   et al., 2014, 2016 and 2022; Tavani and Granado, 2015). Since rift basins are typically segmented by interacting basement faults and slip transfer systems, (e.g., Gibbs, 1984; Morley et al., 1990; Gawthorpe and Hurst, 1993; Coward, 1995) salt flow and associated sediment distribution may be significantly modified, departing from simpler 2D models. Evacuation of salt in
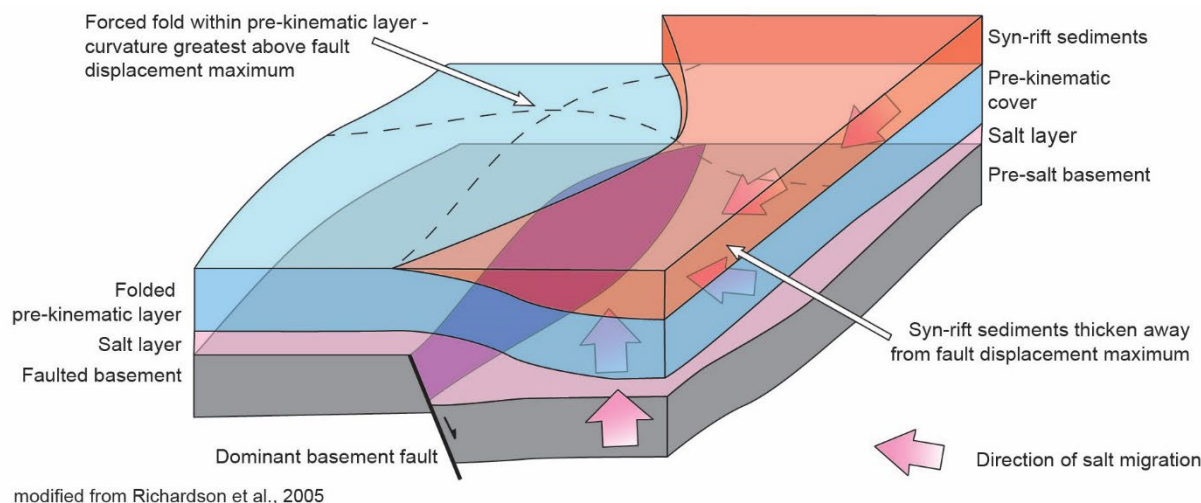
Figure 1. Block diagram illustrating the structural style of decoupled extensional rift half-graben with thick early syn-rift salt, modified from Richardson et al. (2015).

rift basins by differential sedimentary loading upon crustal extension may significantly assist in creating accommodation space (e.g., Stewart et al., 1996, 1997; Dooley et al., 2003, 2005; Richardson et al. 2005), but also obscures the subsidence patterns of the pre-salt basement (e.g., Moragas et al., 2018; Strauss et al., 2021) as well as thermal records (Lescoutre et al., 2019). When extension is coeval to salt evacuation produced by differential sedimentary loading, the geometry of the hanging wall syn-rift depocenters may strongly depart from classical wedge-like basins thickening into active basement faults, obscuring the pre-salt basement structural style (e.g., Richardson et al., 2005; Ferrer et al., 2016, 2022, Roma et al., 2018; Granado et al., 2021). During shortening related to plate convergence, basement faults may be reactivated to different degrees, while the post-salt stratigraphy is usually sheared off from its autochthonous rifted basement. When this is the case, the original relationships between the post-salt stratigraphy and the basement structures responsible for crustal thinning may not be directly observed (e.g., Callot et al., 2012; Mencós et al., 2015; Muñoz et al., 2018; Granado et al., 2019 and 2021; Snidero et al., 2019; Célini et al., 2020). Just as extensional faults play an important role during subsequent shortening, transfer zones also may exert a strong control, leading to structurally complex 3D patterns of deformation, erosion, and sediment dispersal, as well as the associated salt flow patterns. Indeed, there are few works of natural case studies dealing with how segmented rift systems and associated basins have been incorporated into contractional fold-and-thrust belts (e.g., Beauchamp, 2004; Mencós et al., 2015; Muñoz et al., 2018). This is of particular importance when early salt structures, such as salt diapirs or salt sheets, have previously formed during periods of active crustal extension flanking and bounding sedimentary depocenters.

There is a substantial number of scaled physical analogue modeling studies dealing with extension and inversion of rift basins (Koopman et al., 1987; Brun and Nalpas, 1996; Buchanan & McClay, 1991, 1992; McClay, 1989; 1995; 1996; Gartrell et al., 2005; Panien et al., 2005; Schreurs et al., 2006; Konstantinovskaya et al., 2007; Ferrer et al., 2016; Granado et al., 2017; Zwaan et al., 2022). However, few of them have focused on the influence of interaction between individual laterally segmented syn-rift basins across transfer zones in salt-bearing rift systems. The use of silicone as weak points within the middle and lower crusts instead of a coulomb analogue material such as sand significantly changes the deformation style in the overlying sand layers, and the resulting basin geometries (e.g., Brun and Beslier, 1996). Other programs modeled grabens and half-grabens over rigid basement blocks, which significantly force the basin inversion style (e.g., Burliga et al., 2012; Ferrer et al., 2016 and submitted; Moragas et al., 2017; Roma et al., 2018a). However, other experimental programs provide key insights into the styles of salt diapirs that develop along the margins of syn-extensional depocenters, the role of extensional salt structures in absorbing deformation early in shortening and the reactivation of welds as thrusts (i.e., *thrust welds*) during shortening of

individual half-grabens (i.e., Dooley et al.,2003, 2005; Moragas et al., 2017; Stewart, 2017; Roma et al., 2018a; Hansen et al., 2021; Ferrer et al., *submitted*; Miró et al., *this special issue*; Ferrer et al., *this special issue*).

70   By controlling the modelling parameters, physical analogue models can provide structurally balanced and scaled solutions aiding in the construction of geological and geo-seismic sections. In this work, we describe an experimental program formed by three analogue models of extension followed by contractional deformation, without and with syn-contractional sedimentation (see Tables 1 and 2). Our models aim to answer a series of timely questions related to the formation and deformation of laterally segmented salt-bearing rift basins and investigate the following points: i) the geometry and distribution

75   of syn-rift depocenters, ii) structural geometries and stratigraphic architectures in section and map view, and iii) the contractional basement structure and geometry of the thrust wedge. We also investigate the distribution and geometry of salt welds after extension and shortening, and the control of early salt structures and syn-contractional sedimentation on the geometries and kinematics of the developing fold-and-thrust belt. Our modeling results are compared to natural systems characterized by different degrees of structural reactivation, and salt-detached shortening such as the Northern Lusitanian

80   Basin offshore Portugal or the Southern Pyrenees. Traditionally, these salt tectonic provinces have been important to the exploration and production of hydrocarbons. While this is still the case, these provinces are now of importance to the energy transition within the European Union, and across the globe (i.e., European Commission, 2021; Duffy et al., 2021). Extensional salt tectonic provinces may provide the correct setting for the energy storage of hydrogen, compressed air, natural gases, and the long-term storage of CO_2, while their inverted counterparts may provide untapped potential as sources of geothermal energy

85   (e.g., Gasanzade et al., 2021; Martin-Roberts et al., 2021; Alves et al., 2022; Miocic et al., 2022).

Table 1. Experimental models described in this paper.

Experimental Model	Modelled process	Total Extension	Total Shortening
Model 1	Extension	15 cm	
Model 2	Extension + Shortening	15 cm	25 cm
Model 3	Extension + Shortening with syn-contractional sedimentation	15 cm	25 cm

2 Analogue Modelling Program

2.1 Experimental modeling materials and scaling parameters

The goal of the experimental program is to model the formation and contractional deformation of two salt-bearing half-graben
90   basins segmented by an intervening transfer zone. The models were constructed using modelling materials suitable to simulate upper crustal deformation (see Davy and Cobbold, 1991; Weijermars and Schmeling, 1986; Schellart, 2000; Dell'Ertole and Schellart, 2013), and following rigorous principles of dynamic scaling (Table 1). Dry well-sorted quartz sand (i.e., 98% pure silica) with an average grain size of 199 μm, a mean coefficient of friction (φ) of 0.6, and an average angle of internal friction (ϕ) of 34º, a bulk density of 1500 kg/m^3 and cohesive strength of ~55 Pascals was used (Ferrer et al., 2017). Sand displays an

95   elastic/frictional plastic behavior with transient strain hardening prior to transition to stable sliding (e.g., Lohrmann et al., 2003; Adam et al. 2005), being a reasonably good mechanical analogue of upper crust brittle rocks. The material used to simulate rock salt was Rhodosil GUM FB from Bluestar Silicones, a transparent viscous polydimethylsiloxane silicone polymer with a density of 972 kg/m^3 at room temperature and a viscosity of 1.6 x 10^{-4} Pa·s when deformed at an experimental strain rate of 1.83 x 10^{-4} cm/s (Ferrer et al., 2016; Table 2). The polymer behaves as a near-Newtonian fluid having very low yield strength

100   and a stress exponent *n* of nearly 1 at the above-mentioned experimental strain rate. Near-Newtonian silicone polymer can be assumed as a reasonable first order approximation of salt rheology for analogue modelling experiments (Dell'Ertole and Schellart, 2013). Hereinafter, the term model salt will be used as a synonym to silicone polymer and the standard salt tectonics terminology used when describing polymer-related structures.

Table 2. Scaling parameters used in the experimental program.

Quantity	Model	Nature	Scaling ratio
Thickness			
Sand overburden	20–60 mm	2–4 km	1.0×10^{-5}–1.5×10^{-4}
Salt/polymer	10 mm minimum	1000 m	1.0×10^{-5}
Length	1 cm	1 km	1.0×10^{-5}
Density			
Overburden	1500 kg m^{-3}	2700 kg m^{-3}	0.55
Model salt/polymer	972 kg m^{-3}	2200 kg m^{-3}	0.44
Density contrast	528	500	1.05
Polymer layer viscosity	1.6×10^{-4} Pa s	10^{-18}–10^{-19} Pa s	1.6×10^{-14}–1.6×10^{-15} Pa s
Overburden coefficient friction	0.7	0.8	0.87
Gravity acceleration	9.81 m s^{-2}	9.81 m s^{-2}	1

2.2 Experimental set-up and procedure

The experimental program consists of three models (Table 1): Model 1, as the baseline model, involves rifting of the salt-bearing segmented rift system. Model 2 comprises rifting and inversion of the rift system, and Model 3 involves rifting and inversion with syn-contractional sedimentation.

The experimental set-up uses modelling procedures similar to those reported on Dooley and Hudec (2020). The set-up was built on a metal rig with maximum dimensions of 114 cm long by 50 cm wide and 30 cm tall. The model boundaries were laterally set by glass walls and moveable backstops at either end (Fig. 2). The basal set-up of the model consisted of a 30 cm long by 50 cm wide central latex rubber sheet located in the center of the model and attached to a 35 cm long metal base plate on one side and a non-deformable (under modelling conditions) mylar plastic sheet on the other side (Fig. 2). The metal plate and mylar sheet were attached to the moveable backstops. Extension and shortening were achieved by computer-controlled motor-driven worm-screws that pulled or pushed the moveable backstop at the required velocities (see below). A 2 mm thick, layer of polymer covered the basal plate. It served, first, as a basal detachment to accommodate the transference of deformation from the moving walls during extension and shortening, and second, it absorbed any undesired deformation of the rubber sheet (e.g., McClay et al., 2002; Amilibia et al., 2005; Dooley and Hudec, 2020). The model set-up does have limitations, however. Extension focused proximal to both moving backstops. As a result, marginal grabens and minibasins developed on either side of the model.

In our experimental program, polymer seeds placed within the basement sand pack were used to nucleate listric faults and associated half-graben geometries (Fig. 2). Dooley and Hudec (2020) used rectangular prisms of polymer that resulted in the development of grabens. We used triangular polymer prisms to constrain the development of listric faults and the sense of rotation of hanging walls as extension increases. The triangular prisms measured 15 cm long, 7 cm wide, and 4 cm tall in the highest part. The polymer seeds were laterally and longitudinally offset from each other to promote the development of a transfer zone between the fault segments nucleated at each seed. The basal set-up and the two polymer seeds were buried by 9.4 cm thick sand pack simulating the basement (i.e., white sequence in Fig. 2a). The upper part of the sand pack consists of a layered sequence of 2 mm thick blue-white-grey sand layers (Fig. 3). It is important to note that these silicone seeds do not represent preexisting salt structures, but instead represent inherited zones of weakness in the crust.

The different evolutionary stages of the sandbox models were indicated by a specific color sand pack (Fig. 3); the rifting stage comprised three phases. In Phase 1, the basement sand pack was extended to create syn-rift basins above the polymer seeds and a transfer zone in between. Extension was achieved by pulling both moveable walls at a combined velocity of 2.78 x 10^{-4} cm·s^{-1}. Consequently, moving walls stretch the rubber sheet in the center of the model, focusing extensional deformation in
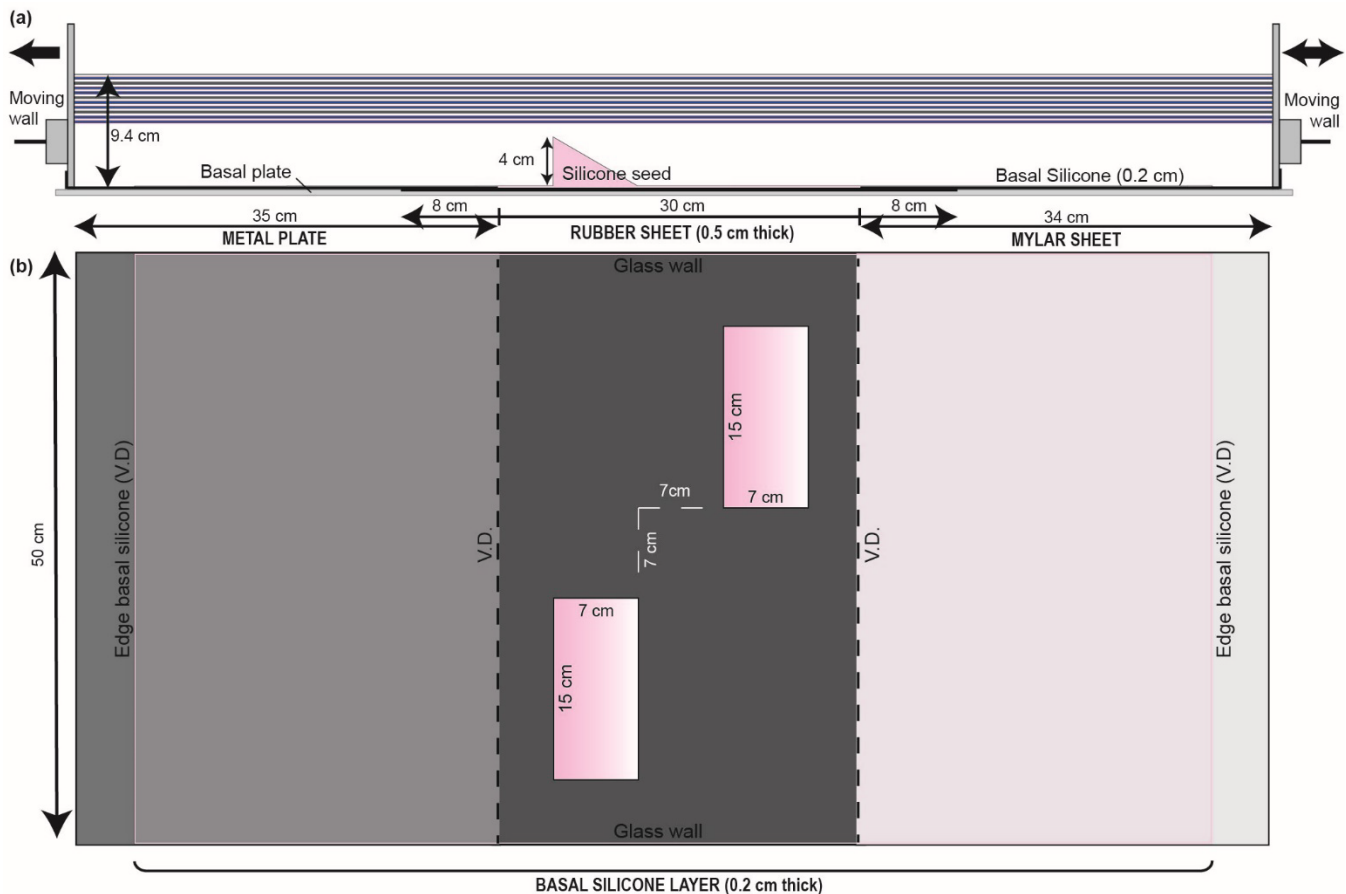
Figure 2. Experimental set-up. (a) Section view of model set-up through one of the silicone seeds illustrating the placement of the triangular prism within the basement sand pack on top of the basal set-up. (b) The plan view figure illustrates the organization of the basal set-up materials. V.D. stands for velocity discontinuity; these discontinuities are present at the edges of the rubber sheet where it connects to the metal plate and mylar sheet. The basal silicone layer that covers the basal set-up is 0.2 cm thick and extends across the entire set up. The two prismatic silicone seeds are located within the rubber sheet and are offset from each other by 7 c in the horizontal and vertical directions.

the overriding sand pack and stretched and thinned the silicone seeds, which localized listric faults and the development of half-grabens (Fig. 3b). Models underwent a total of 9 cm of extension during this first phase.

During Phase 2, the entire model was covered by a layer of syn-rift model salt with a minimum thickness of 10 mm above the basement highs. The polymer was added in pieces and allowed to homogenize for 48 hours until the layer obtained a completely horizontal surface devoid of air bubbles. The model salt was covered by a regional 4 mm thick pair of white and light blue sand layers (referred to the pre-kinematic layer; Fig. 3a) simulating a pre-rift unit.

Phase 3 consisted of six episodes of extension with a velocity rate of 1.67×10^{-4} cm·s^{-1} (slower than Phase 1) each of these followed by deposition of alternating layers of white and red sand to produce loading of the underlying model salt. After the deposition of each layer, models were left for sedimentary depocenters to downbuild, to sink into the salt forming minibasins (e.g., Rowan and Vendeville, 2006; Santolaria et al., 2021), before the next episode of extension. For each layer, sand was added in the center of the lows created by the pulse of extension. Downbuild time for each syn-rift layer lasted from 15h maximum, to 8 h minimum. For the first two syn-rift layers, the regional elevation of sedimentation was maintained at the top
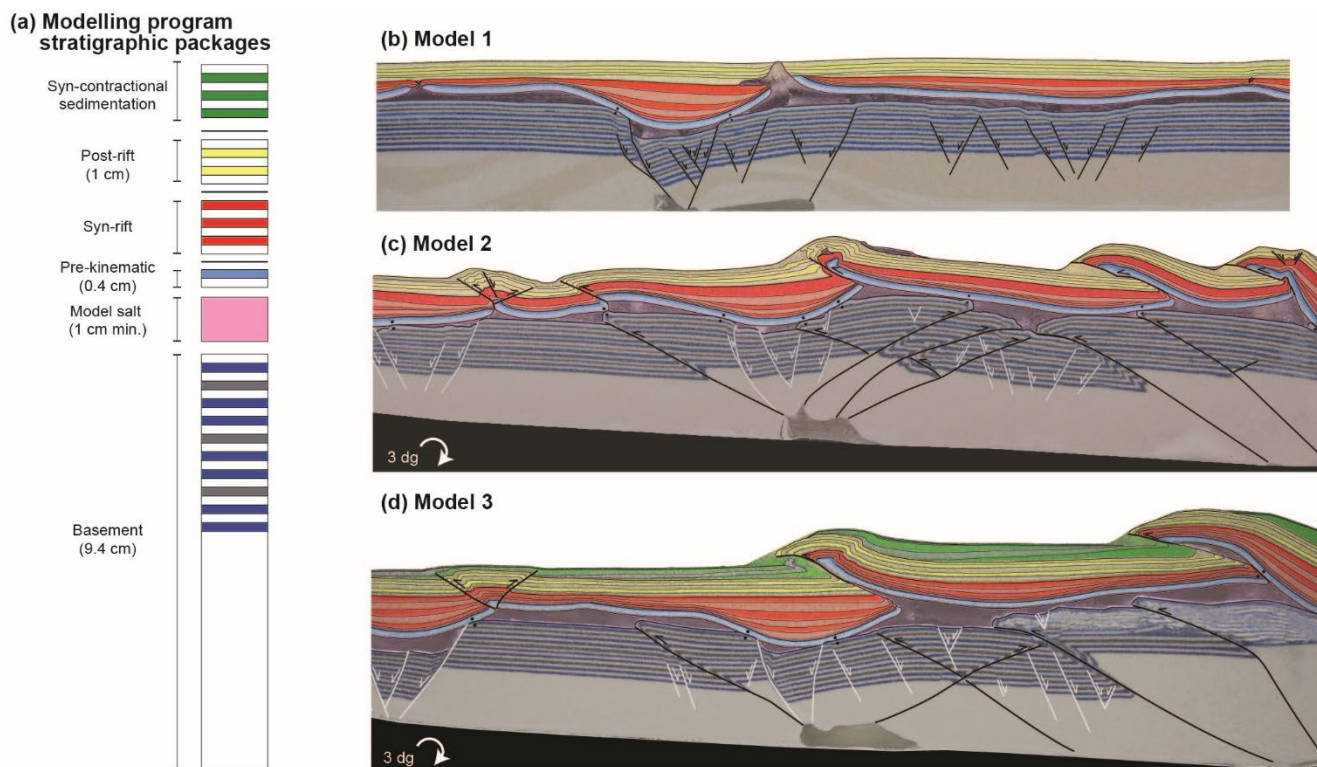
Figure 3. Experimental tectonostratigraphic units and final distributions through each model. (a) Schematic stratigraphic column
of the tectonostratigraphic sand packages and their representative colors. (b) Representative cross section through Model 1 showing
the distribution of the individual sand packages after the deposition of the post-rift succession. (c) Representative cross section
through Model 2 showing the distribution of layers at the end of shortening. (d) Representative cross section through Model 3 at the
end of shortening with the addition of syn-contractional sedimentation.

of the pre-kinematic sand pack. After that, the regional was raised 1 mm for each syn-rift sand layer to preserve those structures
formed by model salt inflation and prevent its extrusion. The surface of the model was leveled using a scraper after the
deposition of each sand layer to keep up with the regional elevation. Leveling caused erosion on the crests of positive relief
caused by salt inflation. The rate of syn-rift sedimentation increased with each layer as differential sedimentary loading
increased the rate of downbuilding and extrusion of model salt from underneath the main depocenters.

At the end of the extension, the entire model was covered by a 10 mm thick post-rift succession of alternating 2 mm thick
layers of white and yellow sand (Phase 4). The layers in this succession were deposited at the same time. Model 1 was stopped
after the addition of the post-rift succession and used as the baseline model for the shortening experiments (Fig. 3).

Lastly, models 2 and 3 were shortened producing the inversion of the segmented extensional basins (Phase 5). Before the onset
of shortening, the deformation rig was tilted 3° towards the hinterland to favor the model attaining its critical taper required to
initiate the basal sliding of the thrust wedge with the least internal deformation possible (i.e., Chapple, 1978; Graveleau et al.,
2012). Shortening was accomplished by moving one wall exclusively (i.e., push from behind model experimental design) to a
maximum of 25 cm of shortening with a velocity of 1.67×10^{-4} cm s^{-1}. Model 2 was shortened without erosion or addition of
syn-contractional sand. Conversely, Model 3 was shortened with the addition of alternating green and white syn-contractional
sand layers. Syn-contractional sand layers were added every 3.6 cm of shortening, raising the regional 2 mm for each new
layer. During shortening, extruded model salt was removed periodically from the surface simulating erosion.

2.3 Data capture and analytical techniques

Overhead high-resolution time-lase photographs were taken every 90 seconds by a computer-controlled digital camera to record the kinematic evolution of the experiments. Videos from the time-lapse photos of each model have been generated (see Supplementary Material). In order to simplify the description of the experimental results, the cover structures have been named according to their time of development and structural style (i.e., T for thrusts, BT for back thrusts, and P for pop-up structures, 180 G for grabens).

At the end of each experiment, the models were sliced at intervals of 3 mm and photographed. Photos taken of the serial vertical cross-sections were then imported to image-processing software to produce 3D voxel models. These voxels were used to extract virtual section such as inlines and depth-slices for analyzing the 3D structural variation of each model (Dooley et al., 2005; Ferrer et al., 2016; Granado et al., 2017; Santolaria et al., 2021). Voxels were also used to interpret key stratigraphic 185 horizons, fault planes, welds and to extract structure maps and true stratigraphic thickness maps of key sand packages.

3. Experimental Results

3.1 Model 1: Rifting

This section describes the experimental results of the baseline Model 1 to illustrate the three-dimensional geometries, tectonostratigraphic architecture, and the structural styles developed during the basement-involved extensional phases. Serial 190 sections of this model and the virtual sections produced from those highlight the three-dimensional geometries, tectonostratigraphic architecture, and the structural styles developed during the basement-involved extensional phases (Fig. 4). Top view photographs (Fig. 5) and the time-lapse video (see Supplementary Material for Model 1) illustrate the evolution of the model surface through extension, as well as the erosional leveling of the cover sequence and the inflation and extrusion of model salt.

195 Cross-sections show master basement faults with a concave upwards listric geometry rooted at the highest point of the polymer seeds (MF1 and MF2 in Figs. 4a, c). These faults trend orthogonal to the extension direction, while their lateral extension is imposed by the width of the polymer seeds. The triangular shape of both seeds constrains the development of another listric fault in the footwall of the master ones. Slip attained by the master faults produces half-grabens above both polymer seeds, characterized by hanging wall rollover anticlines. In the case of MF2, this rollover has a crestal collapse graben associated. 200 The rollover anticlines are also bound by antithetic extensional faults developed at the other tip of the polymer seeds (Fig. 4a, c). MF1 attains more slip than MF2, and consequently, both faults create different accommodation space at the syncline minibasins developed on their downthrown hanging walls. Conversely, the intervening transfer zone in between MF1 and MF2 is characterized by a dense array of left- and right-dipping extensional faults with limited displacement describing a central horst bounded by two grabens (Fig. 4b).

205 While the structural style of basement is characterized by faulting and rollover anticlines, the salt overburden is characterized by decoupled deformation in the form of folding (i.e., broad synclines and anticlines) and salt structures (Fig. 4a to c). Synclinal basins develop above the hanging walls of MF1 and MF2 (mb1 and mb2, respectively). These synclinal depocenters are filled by syn-extensional layers that pinch out laterally. The model salt layer shows important thickness differences, being totally depleted above the major basement faults to thickened by inflation in the footwall of these faults and above the basement 210 rollover hinges (Fig. 4 a and c). A diapir developed by crestal extension and erosion of the salt inflated anticline developed above the rollover anticline of MF1, allowing the extrusion of a salt glacier (Fig. 4c). In the transfer zone, inflated salt above the basement horst separates the lateral terminations of both synclinal minibasins (Fig. 4b).

Virtual inlines (Fig. 4 d to f) show the geometry of the syn-rift minibasins along strike, the distribution of model salt, and the basement fault plane intersections. In these sections, the syn-rift minibasins display similar geometries to those displayed in
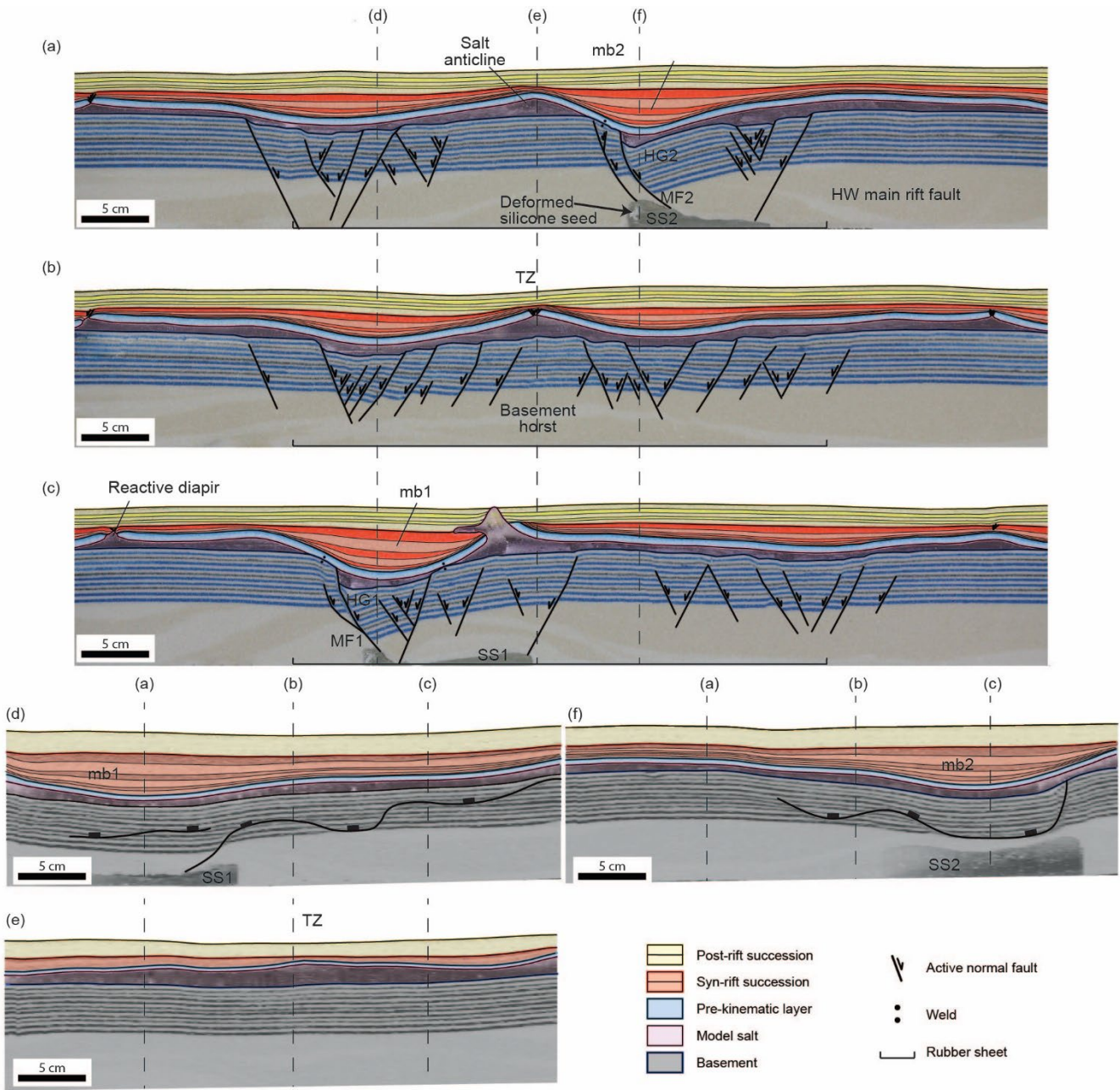
Figure 4. Interpreted representative cross sections (a-c), and virtual inlines (d-f) through the central minibasins (mb1 and mb2) and the basement transfer zone of Model 1. See figure 5c for the location of each section.

the cross-sections, with laterally lapping early syn-rift layers, and their thickest succession coincident with the center of the minibasin. The distribution of model salt is roughly even across the inlines passing through the minibasins depocenters. By contrast, models salt is thickest and shows an uneven distribution through the transfer zone, where the syn-rift succession is thinnest (Fig. 4e).

Early thick-skinned extension after deposition of the pre-kinematic layer triggered model salt movement and formation of drape folds above the major basement faults, while salt inflation occurred at the basement rollover hinge (Fig. 5a). Some grabens developed along the crest of developing salt anticlines near the edges of the model (Fig. 5a). As extension increased,
225   migration of model salt from below the synclines towards the hinge of the basement rollovers increased producing significant inflation in salt-cored anticlines (blueish colors in Fig. 5b). At the same time, drape monoclines formed above major basement faults also allowing the development of salt-inflated anticlines in the footwall of those faults (Figs. 4a, 5b, and 6c). The stretching produced at the crest of some of these anticlines allow the development of grabens that thinned the overburden (i.e., mb1, Fig. 5b). In addition, the relief generated by salt inflation favored the erosion of many of these anticlines (blueish colors
230   in Fig. 5b). After 4.2 cm of extension, the syncline basins propagate laterally. At this point a depressed zone separated the anticline developed at the hinge of the basement rollover related to mb1 and the one developed above the footwall of MF2 (Fig. 5b). As deformation progressed, the syncline basins become wider and gentler (Fig. 5c) as the last broadly uniform syn-rift layers indicate (Fig. 4a-c). The sedimentation rate applied to the model resulted in the burial of most of the salt-cored anticlines, and a diapir only developed during this late extensional stage (Fig. 5c). This diapir formed by a combination of
235   crestal stretching and erosion as the unconformity between pre-kinematic and syn-kinematic layers indicates at both flanks of the structure (Fig. 4c). A salt sheet extruding towards the inner part of the syncline basin formed during the end of rifting (Fig. 5c) and the diapir grew passively during the deposition of the post-rift sand pack (Fig. 4c).

Thickness of the post-rift layers is quite uniform. However, close to the model salt sheet (Fig. 5c), thickness of the first post-rift layer increases towards the extruding model salt, below which the base of mb1 is welded to the top of the basement (Fig.
240   4c). Timing of welding is thus coincident with the end of rifting for the footwall welds, while welding of mb1 below the thickest post-rift succession occurs during post-rift salt extrusion associated with sediment loading.

The top basement structure map shows two main structural lows associated with the displacement maxima of the master faults above the silicone seeds (Fig. 6a). Half-graben 1 propagated along strike across the whole model width (Fig. 4 a-c). This is probably related to the presence of the underlying velocity discontinuity (V.D. in Fig. 2) that favors extension localization,
245   lateral slip transfer along the strike of the silicone seed, and the formation of the largest depocenter of Model 1. Conversely, extension along MF2 produces a more diffuse structural pattern, with one largest depocenter right of the master fault, and another depocenter shifted to the bottom right of the model (Fig. 6a). As shown by the structural maps (Fig. 6a), the basement top at the transfer zone lays deeper than the basement highs.

A true thickness map of the autochthonous model salt (i.e., TST map on Fig. 6b) depicts the position and shape of the welded
250   areas of minibasins 1 and 2 ("W" in Fig. 6b). The map also shows thinning and welding of the autochthonous salt at the tip of the footwall blocks of the extensional faults (i.e., nearly welded areas; compare Fig. 4 and Fig. 6d). An apparent single salt anticline continues from the hanging wall of MF1 links with the salt anticline in the footwall of MF2 across the transfer zone (Figs. 6c and d).

Distribution of the syn-rift succession thickness is illustrated on the true stratigraphic thickness map (i.e., TST map on Fig.
255   6c). The map shows that the syn-rift depocenters display an elliptical pattern, whose thickness distribution follows the location and trend of the basement extensional faults. A ridge of thin syn-rift sediments links the footwall of MF2 with the hanging wall of MF1, marking the trend of a salt anticline across the transfer zone. Towards MF1 hanging wall the salt anticline becomes a salt-extruding wall (Fig. 6c). Additional syn-rift depocenters also follow the trend of the basement top and occur shifted from the position of mb1 and mb2. These depocenters are proximal to the velocity discontinuities (i.e., edges of the
260   rubber sheet).
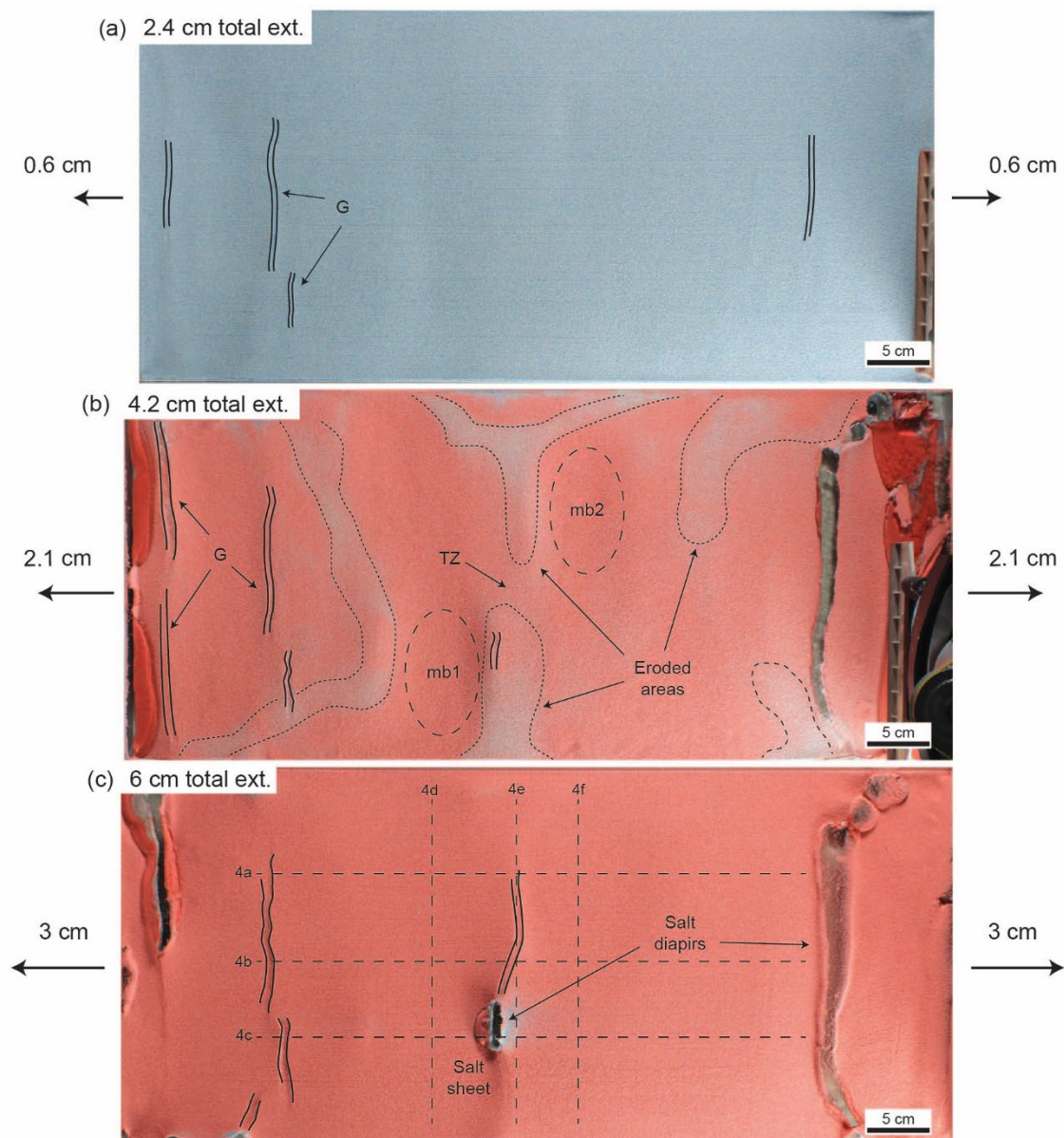
Figure 5. Overhead views illustrating the surface evolution of Model 1 after 2.4, 4.2 and 6 cm of extension, respectively. (a) Incipient grabens developed during the early extension (2.4 cm) at the top of the pre-kinematic overburden; (b) syncline basins (mb1 and mb2) development constrained by the slip of basement faults rooted at the polymer seeds during mild extension. Salt-inflated areas (blue-reddish color) are locally eroded; and (c) a salt sheet extrudes from a passive diapir developed by erosional piercement during the late extension. During this stage, synclinal basins are wider. Abbreviations: G for graben; TZ for transfer zone.
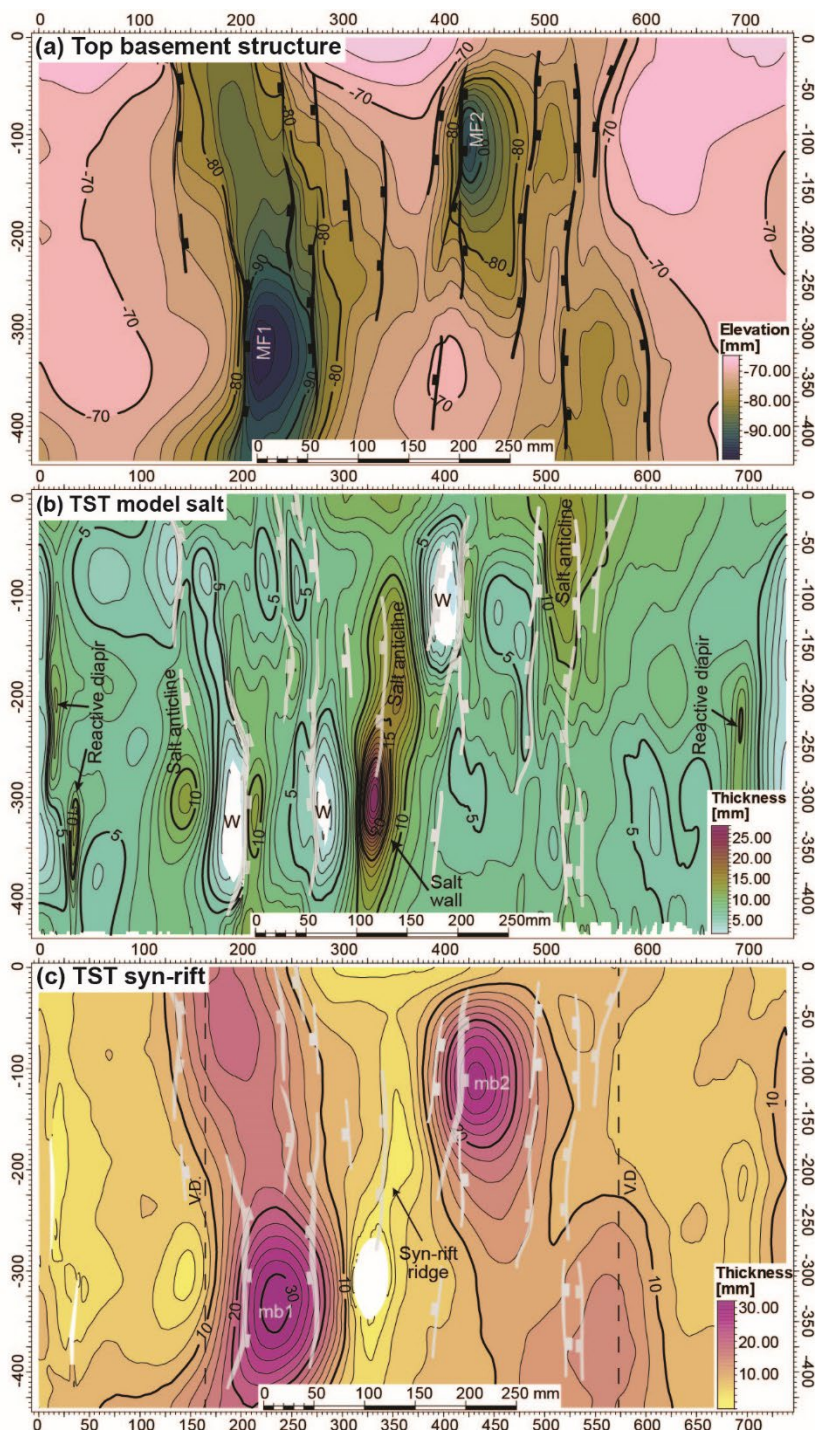
Figure 6. Structure and true stratigraphic thickness (TST) maps of key horizons in Model 1: (a) Top basement structure map, (b) TST autochthonous salt map, and (c) TST syn-rift map (W represents the welded area where salt has been depleted). Light gray lines in figures b and c represent the basement structures.

3.2 Model 2: Shortening without syn-contractional sedimentation

This section describes the results of Model 2, which was subjected to 25 cm of shortening (Fig. 7). Besides the periodic removal of extruded silicone, no addition of syn-contractional surface processes (i.e., erosion or sedimentation) were performed on the
275 model. The serial sections highlight the three-dimensional geometries of deformed salt structures and the involvement of the pre-salt basement in a broadly foreland propagating sequence of thrust imbrication (Figs. 7a-d). Top view photographs (Fig. 8) and time lapse videos (see Supplementary Material for Model 2) illustrate the kinematics of the salt-detached thrust system, and the contractional deformation of salt structures developed during previous extensional phases. In both the sections and top view photographs, the structures in the cover are labeled by a letter representing structure type followed by a number
280 representing the order in which the structures developed. Degradation of the frontal limbs of surface-breaching thrust-related folds is common throughout the modeling.

During shortening the contractional deformation has also been decoupled along the syn-rift model salt. Underneath, the basement-involved thrust system has been detached along the basal silicone layer truncating the previously developed extensional faults. However, the master basement extensional faults have been partially reactivated along the shallow dipping
285 portions, as the main thrusts have also been nucleated in the silicone seeds, thus reproducing inversion tectonics geometries, such as short-cuts (Fig 7. a-d). The distribution of the model surface elevation relates to the inversion of these basement extensional faults. Thus, the lowest regional elevation is located in the footwall of the thrusts inverting the master extensional faults (Fig 7. A, c). The section through mb2 displays a broad hinterland plateau in the hanging wall of the inverted MF2, which shows a short-cut in the upper part of extensional MF2 (Fig. 7a). The hinterland pre-salt basement is also affected by
290 two foreland propagating thrusts which transfer the displacement upwards into the syn-rift model salt; late back thrusts cut these thrusts. The contractional structure of the post-salt succession is represented by salt-detached thrusts and back thrusts and related folds (Fig. 7a). Unlike the basement structure, there is not a predominant vergence. After 25 cm of shortening mb2 remains welded to the basement at two points, the footwall and the hanging wall of the inverted MF2 basement fault (i.e., its original location according to Model 1). Above, the thinner syn-rift cover sequence deposited on the footwall of the MF2 is
295 back thrusted over the syn-rift depocenter of mb2, generating the highest structural elevation of the section. Additional structures are: a pop-up in the foreland related to the squeezing and secondary welding of diapirs (P4); a salt-detached back thrust transporting mb2 with a frontal pop-up structure (BT3); a hinterland-dipping thrust involving the marginal syn-rift minibasin (T1); triangle zone welded to the basement buried below resedimented post-rift sediments and allochthonous salt sheet (Fig. 7a).

300 The section along the basement transfer zone is characterized by a smoother change in the topography in comparison to the previous section (Fig. 7b). The basement structure corresponds to an imbricated wedge of thrusts and back thrusts, cutting through inherited extensional faults. The section also displays two structural highs related to salt-detached structures. The regional elevation is controlled by the basement thrust system, however, the topographic surface ahead of the frontal thrust system is more gradual than in the previous section (Fig. 7a, b). The detached cover succession in the foreland is characterized
305 by two back thrusts, one formed after the squeezing of a salt wall (BT4) and a back thrust located immediately ahead of the foremost basement thrust tip (BT6). The central salt structure is formed by a fully welded salt wall with a preserved pedestal, flanked by the lateral terminations of syn-rift mb1 and mb2. A salt sheet developed above this structure, with the majority of the salt extrusion flowing towards the hinterland in response to the hinterland-dipping slope. Time of salt extrusion began during the post-rift, as shown by the allochthonous salt deposited on top of the syn-rift succession, and continued to extrude
310 during shortening, until the salt sheet was cut off from its source due to welding. At the hinterland, thrusts and a back thrust interact each other to develop pop-ups and a triangle zone underneath an allochthonous salt sheet (Fig. 7b).

The section through mb1 shows a different topographic distribution than the previous two sections (Fig. 7c). The frontal basement thrust is located further to the left (foreland) because of the inversion of MF1 and its silicone seed (SS2). This seed also controlled the nucleation of a back thrust system which produced the uplift of the former rollover anticline and the
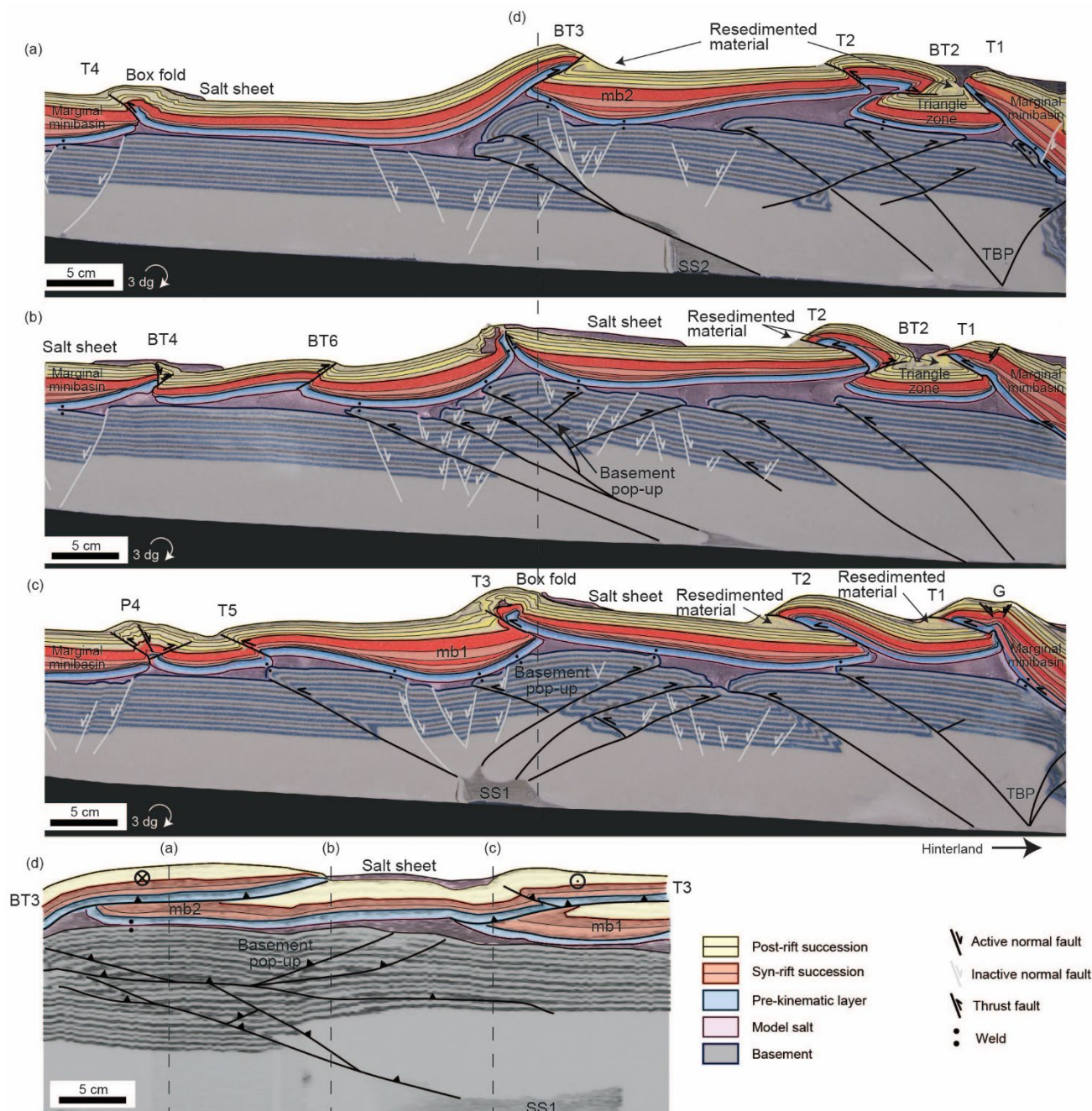
Figure 7. Interpreted representative cross sections (a-c) through the central minibasins (mb1 and mb2) and the basement transfer zone of Model 2, plus a virtual inline through the transfer zone (d). Individual structures in the cover thrust system are labelled according to their timing of kinematic evolution (T – thrust; BT – back thrust; G – graben; P – pop-up structure; SS1, SS2 – silicone seeds). See figure 8d for the location of each section.

315

320   highest structural elevation. The post-salt succession displays a consistent foreland vergence of thrusts and related folds, contrary to the other two sections of Model 2. Mb1 preserved a relatively low structural position at the end of the contractional deformation in the footwall of the thrust that resulted from the break-through of the squeezed salt anticline and related salt structure. In addition, mb1 is welded to the basement at three different points – on the footwall of MF1, and in two places on the hanging wall. Foreland verging thrusts developed in the hinterland part of the model. The marginal minibasin at the rear

325   of the wedge is imbricated on a thrust sheet and folded into two dipping panels: a shallowly-dipping thrust tip, and steeply dipping back-limb. The transition of both panels is marked by a crestal collapse graben structure (Fig. 7c).

A virtual inline through the basement transfer zone shows the lateral stack of the post-salt succession with the reduced syn-rift succession in a hanging wall position of either the thrust or the back thrust (Fig. 7a, c, d). Model salt thickness is thinnest below mb1 and mb2 (even welded below mb2) and thickens in the basement transfer zone with the thickest position along the

330   margin of mb1.

The kinematic evolution of the cover sequence during the shortening phase can be tracked using top view images and time-lapse videos (see Supplementary Material for Model 2, and Fig. 8). The post-salt thrust system developed as a foreland propagating (right to left) sequence, although salt structures were reactivated in the foreland ahead of the thrust front since early stages of shortening (Fig. 8). At the onset of shortening, extensional faults and diapirs occurred in the left margin

335   (foreland) of the model (Fig. 8a). This extensional deformation probably developed in response to the 3° tilt of the deformation rig toward the hinterland. The first thrust (T1) developed in the hinterland against the backstop (Fig. 8a). Time-lapse videos show that salt wall squeezing occurred across the model after about 6 cm of shortening (~25% of total shortening) coeval with the development of the second foreland verging thrust in the hinterland, T2 (Fig 8b and Supplementary Material). The back thrust (BT2) to the right from T2 as can be seen in sections 7a and 7b, are not clearly visible from the top view images, except

340   for a slight indenture in the hanging wall of T2 (Figs. 8b-d). After 12 cm of shortening (~50% of total shortening) thrusts and back thrusts nucleate along the salt walls in the model (Fig. 8c).

The transfer zone between the master extensional faults at the onset of shortening is characterized by the presence of a diapir located at the intersection between the salt anticline developed above the rollover anticline of MF1 and the salt anticline at the footwall of MF2 (compare Figs. 5, 6 and 8). This diapir has been squeezed since early stages of shortening and feeds an

345   allochthonous salt sheet that occupies the structural low between the inverted mb1 and mb2 minibasins (Figs. 7d and 8). As deformation progressed, the back thrust that resulted from the squeezing of the salt anticline in the footwall of MF2 (BT3) and the thrust at the MF1 rollover salt anticline (T3) connect with the salt weld of the squeezed diapir (Figs. 7 and 8). Near the end of shortening, a thrust (T5) and back thrust (BT6) develop in the foreland ahead of the transfer zone (Fig. 8c).

The top basement structure and true stratigraphic thickness (TST) maps of the syn-rift succession and model salt are shown in

350   Figure 9. The top basement structure map shows foreland propagating thrusts. The highest elevation of the basement sits in the center of the model and is the result of the connection of the short-cut of the inverted MF2 fault with the pop-up developed on the previous rollover anticline of MF1 fault. A subtle change of strike and a decrease of structural relief along this high occur in the transfer zone (Fig. 9a). The basement-involved frontal thrust shows a significant change of strike and a resulting concave geometry in map view as a result of the connection of the inverted major extensional faults forward of the transfer

355   zone, contrasting with the more prominent uniform structural trend in the supra-salt succession (Fig. 9b).

The model salt distribution map shows the relationship between the model salt and both the basement and cover thrust systems (Fig. 9b). The salt thickness map reveals that the number of welds increases two-fold in this shortened model. The preexisting primary welds along mb1 and mb2 are more extensive than at the end rifting (Model 1), forming more elongate and wider zones of contact between the cover and basement systems (Figs. 6b, 9b). The preexisting salt walls in the transfer zone and

360   foreland of Model 2 act as sources for salt sheets until they are secondary welded (Fig. 8a-d) and now appear as high amplitude and short wavelength anticlines adjacent to elongated secondary thrust welds (Fig. 9b). The distribution of model salt is influenced by the geometry of the basement and cover thrust systems. The basement thrust fronts can easily be traced in the TST map and the cover thrusts initiate on the areas of early model salt structures (Figs. 9b, 7a-c).
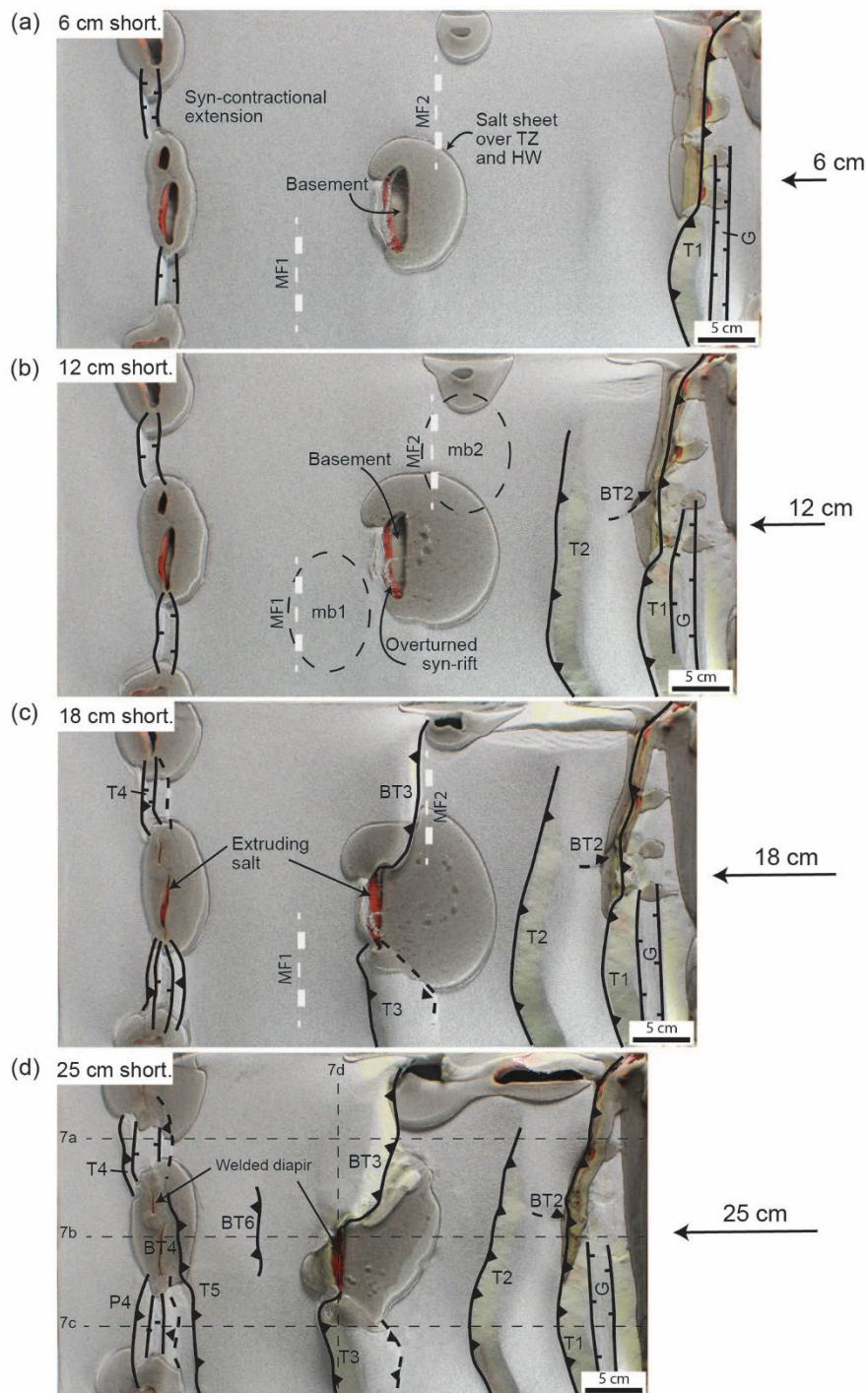
Figure 8. Top-view images illustrating the contractional kinematic evolution of Model 2, including the timing of thrust initiation, model salt extrusion from salt sheets, contractional welding of salt sheets. Abbreviations: short. – shortening, T – thrust, G –graben, BT – back thrust, P – pop-up structure.
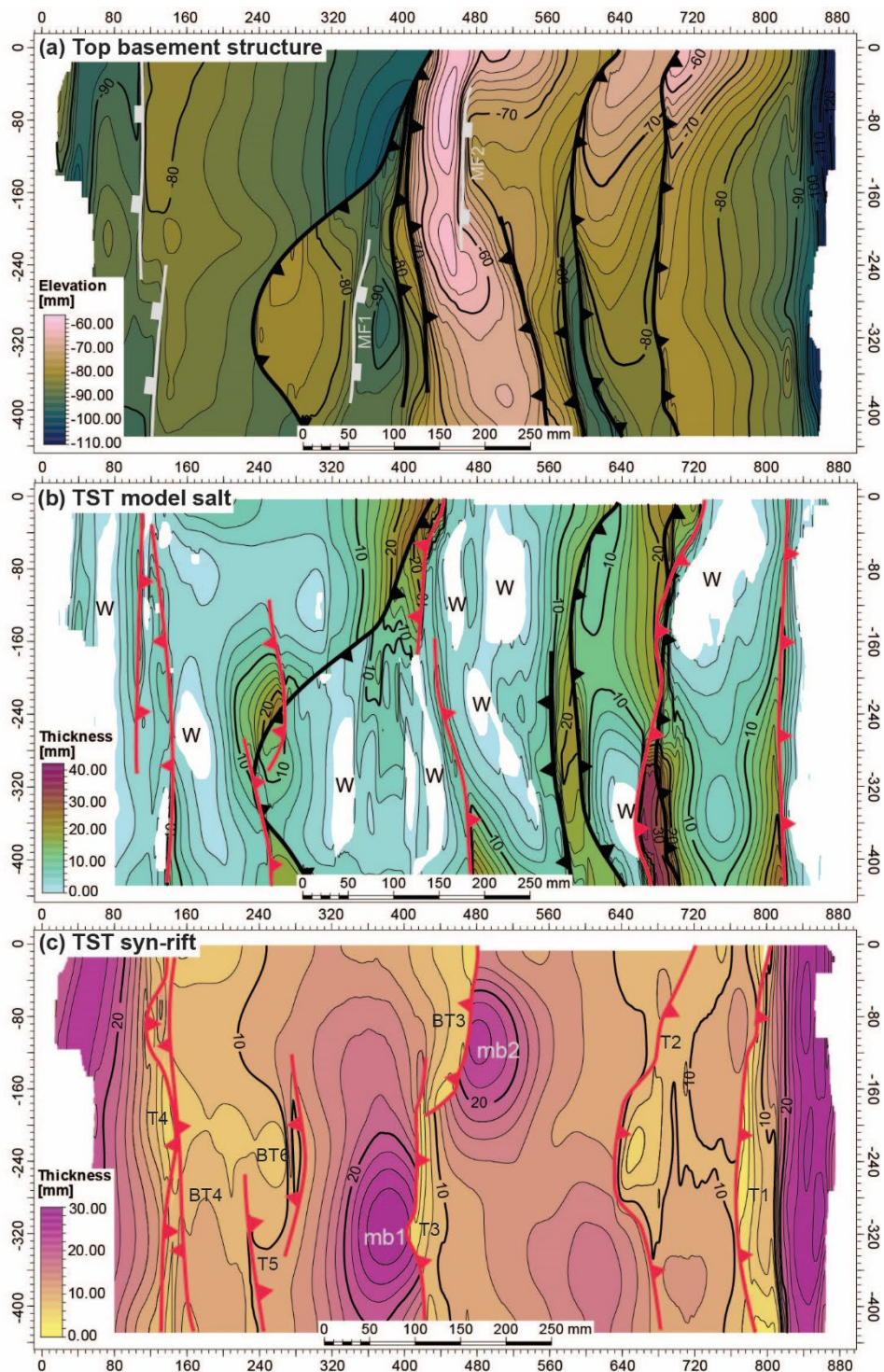
Figure 9. Structure and true stratigraphic thickness (TST) maps of key horizons in Model 2: (a) Top basement structure map, (b) TST autochthonous salt map, (c) TST syn-rift map. Basement thrusts are in black and cover thrusts are in red.

The TST syn-rift map highlights the distribution of the syn-rift succession and location of the cover thrust systems in relation to the syn-rift depocenters (Fig. 9c). Across the model, the syn-rift depocenters remain in the footwalls of the thrusts, except for the marginal minibasin in the hanging wall of T1 which is adjacent to the moving backstop and forms the first cover thrust (T1).

3.3 Model 3: Shortening with syn-contractional sedimentation

Model 3 was subjected to the same extensional and shortening processes as Model 2. In addition to the periodic removal of extruded silicone, syn-contractional sedimentation was added every 6 hours (every 3.6 cm of shortening), while the regional was raised 2 mm for each layer. Serial sections highlight the foreland progradation of a syn-contractional sedimentary wedge that thins towards the foreland, onlapping the underlying salt-detached structures in the cover sequence (Fig. 10). Top view photographs (Fig. 11) and time-lapse videos (see Supplementary Material for Model 3) illustrate the influence of the syn-contractional sedimentation on the kinematics of the salt-detached thrust system, and the contractional deformation of preexisting salt structures. In both the sections and top view photographs, the structures in the cover are labeled with a letter representing structure type followed by a number representing the order in which the structures developed. As in Model 2, degradation of the frontal limbs of surface-breaching thrust-related folds is common throughout.

As in Model 2, the master extensional faults have been reactivated by the nucleation of the thrusts on the silicone seeds. The basement thrust system detaches on the model salt layer, crosscut the minor extensional faults, and control the slope of the model surface (Fig. 10a-c). The surface slope consistently dips to the left across all three sections. In the section through mb2, the frontal thrust reactivating MF2 controlled the location of the syn-contractional depocenter in its footwall and the uplift of mb2 (Fig. 10a). The accommodation space of this depocenter increased by salt evacuation of the former salt inflated area in the footwall of the preexisting MF2 extensional fault (compare Figs. 4a and 10a). Evacuated salt was extruded to form a salt sheet forward of mb2. Uplift of mb2 in the hanging wall of the thrust reduced the accommodation space for the syn-contractional succession deposited above, which contrasts with the thick syn-contractional succession above the thin syn-rift series in the footwall of the thrust, thus reproducing a classical basin inversion geometry, although no extensional faults affected the post-salt succession (Figs. 4a and 10a). The post-salt cover sequence has been decoupled from the basement regardless of whether it has been welded to the basement in multiple places. The foreland propagating thrusts in the cover sequence are sourced by model salt, which has broken through the thrust tips and extrudes on to the surface as allochthonous salt sheets (see Supplementary Material). The footwall and hanging wall cutoffs for thrusts T1 and T3, as well as the thrust welded salt wall, are characterized by reduced stratigraphy of the syn-rift and post-rift successions, demonstrating the presence of inflated model salt in these positions prior to shortening. The thrust tip of T1 is overturned and folded over the underlying syn-contractional sedimentary wedge. The salt wall that developed to the right of mb2 during extension is secondary thrust welded at the pre-kinematic layer while model salt is preserved in the salt stock above the weld (Fig. 10a). A back thrust (BT4) developed in the foreland cover sequence to the right of the welded marginal minibasin. Across the section, the syn-rift minibasins are incorporated in the hanging walls of the thrusts and back thrust.

The section through the basement transfer zone reveals a cover thrust system decoupled from the basement thrust stack. In only one point at the foreland the marginal syn-rift minibasin is welded to the footwall of a preexisting normal fault (Fig. 10b). A significant amount of model salt is present in the section above the basement transfer zone. The basement thrust stack through the transfer zone is characterized by foreland propagating thrusts, unlike the large imbricate thrust fan that occupies the transfer zone in Model 2 (Figs. 7b, 10b).

Along the section through mb1, the basement thrust system extends farther into the foreland by reactivation of the silicone seed related with MF1 (Fig. 10c). Little shortening is taken up by the two thrusts and back thrust that developed in the central area of the section, while the two thrusts that nucleate in the trailing branch point (TBP) accommodate most of the shortening in the basement across this section. Unlike mb2, mb1 has not experienced uplift in the hanging wall of thrust that reactivated MF1, and the depocenter of the syn-contractional succession is located above the minibasin depocenter. The existence of the
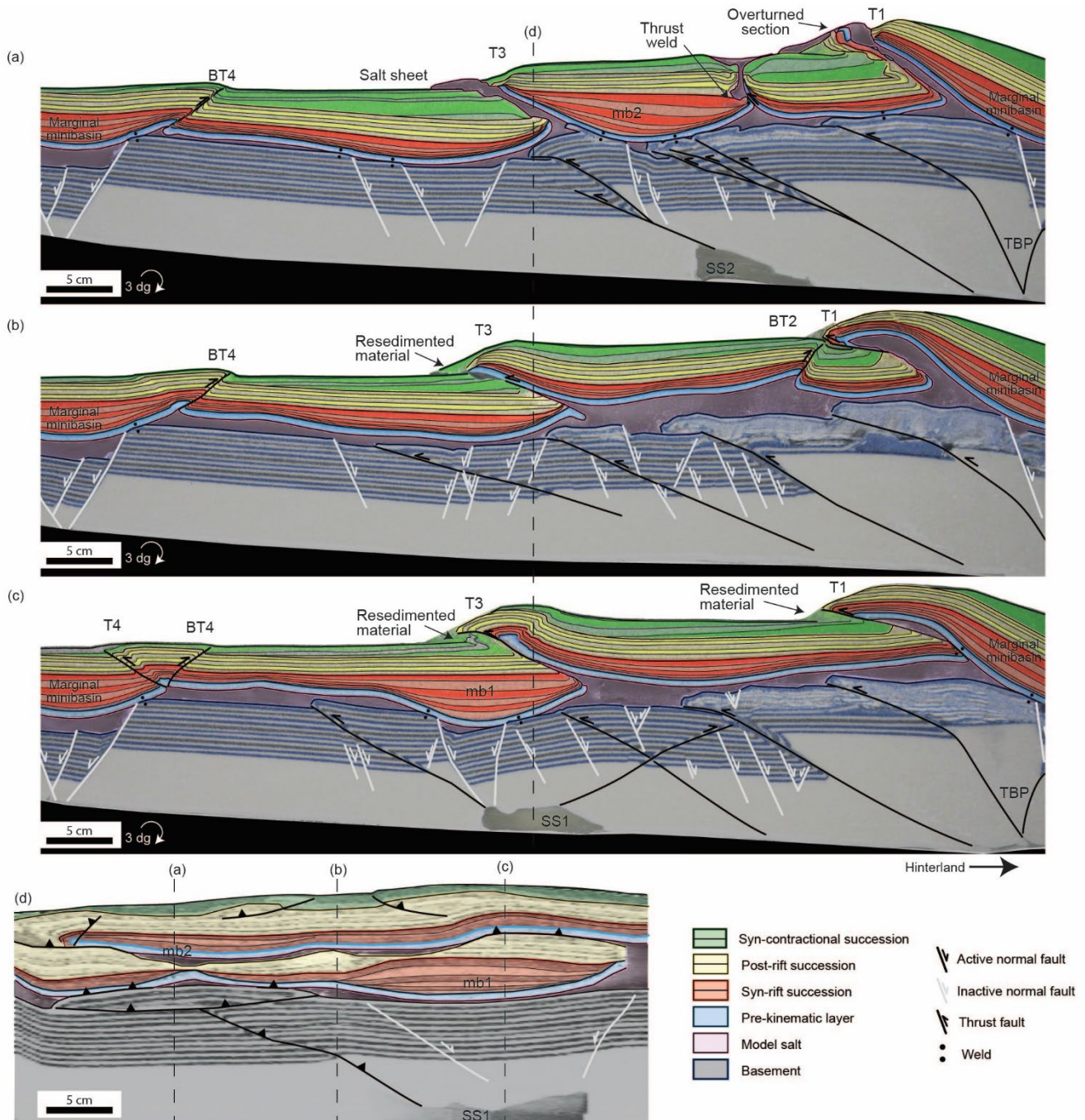
Figure 10. Interpreted representative cross sections (a-c) ad virtual inlines (d) through the central minibasins (mb1 and mb2) and the basement transfer zone of Mode 3. Individual structures in the cover thrust system are labelled according to their timing of kinematic evolution. Abbreviations: T – thrust, BT – back thrust, P – pop-up, TBP – trailing branch point, SS1, SS2 – silicone seeds). See figure 11d for the location of each section.

415

420 basement frontal thrust cannot be inferred from the geometry of the post-salt succession (Fig. 10c). The cover sequence welds to the basement in four locations; one weld per marginal minibasin and two welds along mb1, one weld on to the footwall of MF1 and the other weld on its hanging wall (Fig. 10c). Less model salt is preserved in the cover thrusts in comparison to the other sections across Model 3. The hanging wall of T1 is thrust welded on the lower reaches of its footwall, preserving inflated model salt below the central part of its hanging wall. T3 has no model salt along its base, and the thrust tip is characterized by a pop-up structure above an overturned and folded syn-contractional footwall syncline. The hanging wall of T3 forms a very

425 shallowly dipping panel towards the hinterland, whereas BT3 is not present in this section. Mb1 is welded to the basement in the footwall of T3, and on the footwall of MF1. The foreland-most cover structure in this section developed on the hinterland side of the welded marginal minibasin as well and corresponds to a pop-up structure.

A virtual inline from the 3D seismic volume generated from the sliced sections shows along-strike changes of the geometry of the repeated cover succession (Fig. 10d). The highest basement elevation sits on the left, below mb2, where the cover sequence

430 is welded in two places and does not coincide with the highest structural elevation. Across the inline, the model salt is discontinuous, interrupted by welds at the lower source layer, with a thin allochthonous layer in the central part of the line between the footwall and hanging wall of T3. The syn-contractional sedimentary wedge thins over the crests of the uppermost folds near thrust tips and is thickest in the center of the line.

The kinematic evolution of the cover sequence during the shortening phase can be tracked using time-lapse videos and is

435 illustrated here by top view images (see Supplementary Material and Fig. 11). The post-salt thrust system developed as a foreland propagating (right to left) succession (Fig. 11). At the onset of shortening, syn-contractional extension occurs in the foreland, as in Model 2 (see Supplemental Material for Model 3). Pre-contractional model salt diapirs extruded salt onto the model surface (Fig. 11a). T1 develops in the hinterland proximal to the backstop with an arcuate thrust front. Unlike Model 2 where two thrusts (T1 and T2) develop in the hinterland proximal to the backstop, only one thrust (T1) develops in this region

440 (Figs. 8a, 11a). Only the first two syn-contractional layers are deposited in the hanging wall of T1. As T1 continues to propagate forward, a graben occurs at the crest of the thrust-related anticline. Time-lapse videos reveal that salt wall squeezing occurs at about 6 cm (~25% of shortening) across the entire model (Fig. 11a). The squeezed salt walls nucleate back thrusts (BT2) and thrusts (T3) at around 12 cm (~50% of shortening), and the syn-contractional sedimentary wedge continues to prograde towards the foreland (Fig. 11b). Downbuilding occurs across the transfer zone in response to continued extrusion of model salt from

445 isolated salt plugs (Fig. 11b). By 18 cm of shortening, the individual thrusts nucleated along the salt walls have merged into a single thrust front with small back thrusts and pop-ups developing in the hanging wall (Fig. 11c). The height of the thrust front of T3 is great enough to restrict deposition of syn-contractional sand to its footwall. Continued degradation of the thrust front of T1 and syn-contractional extension on its hanging wall led to model salt piercing in its thrust front near BT2 (Fig. 11c). This led to model salt extrusion that, with further shortening, extends laterally along the T1 thrust front, breaking through more

450 of the front toward the top of the model (Fig. 11d). The foreland pop-up structure, bounded by T4 and BT4, develops at around 20 cm of shortening and creates enough elevation to restrict deposition of the final syn-contractional sedimentary layer in the footwall of T4, along the top of the model, and in the top half of the footwall of BT4 (Fig. 11d). The asymmetry in the deposition of this final layer of sand is attributed to the large volume of extruded model salt coming from salt walls along the model edge.

455 The top basement structure map reveals four structural steps that have decreasing average elevations from right to left (Fig. 12a). The third basement thrust sheet level incorporates MF1 and MF2. Two individual thrust sheets develop on the foreland side of each main normal fault and associated half graben; a lateral ramp in the thrust sheet ahead of MF1 links the thrust sheet with the thrust ahead of MF2.

The map showing the distribution of salt thickness highlights the relationship between the model salt and the thrust systems

460 (Fig. 12b). As in Model 2, the TST salt map reveals that the number of welds increases two-fold during shortening. The pre-contractional primary welds along mb1 and mb2 are more extensive and the welded along the foreland and hinterland sides of both minibasins (Fig. 12b). New primary welds are present along the top half of the model and correspond with the area of
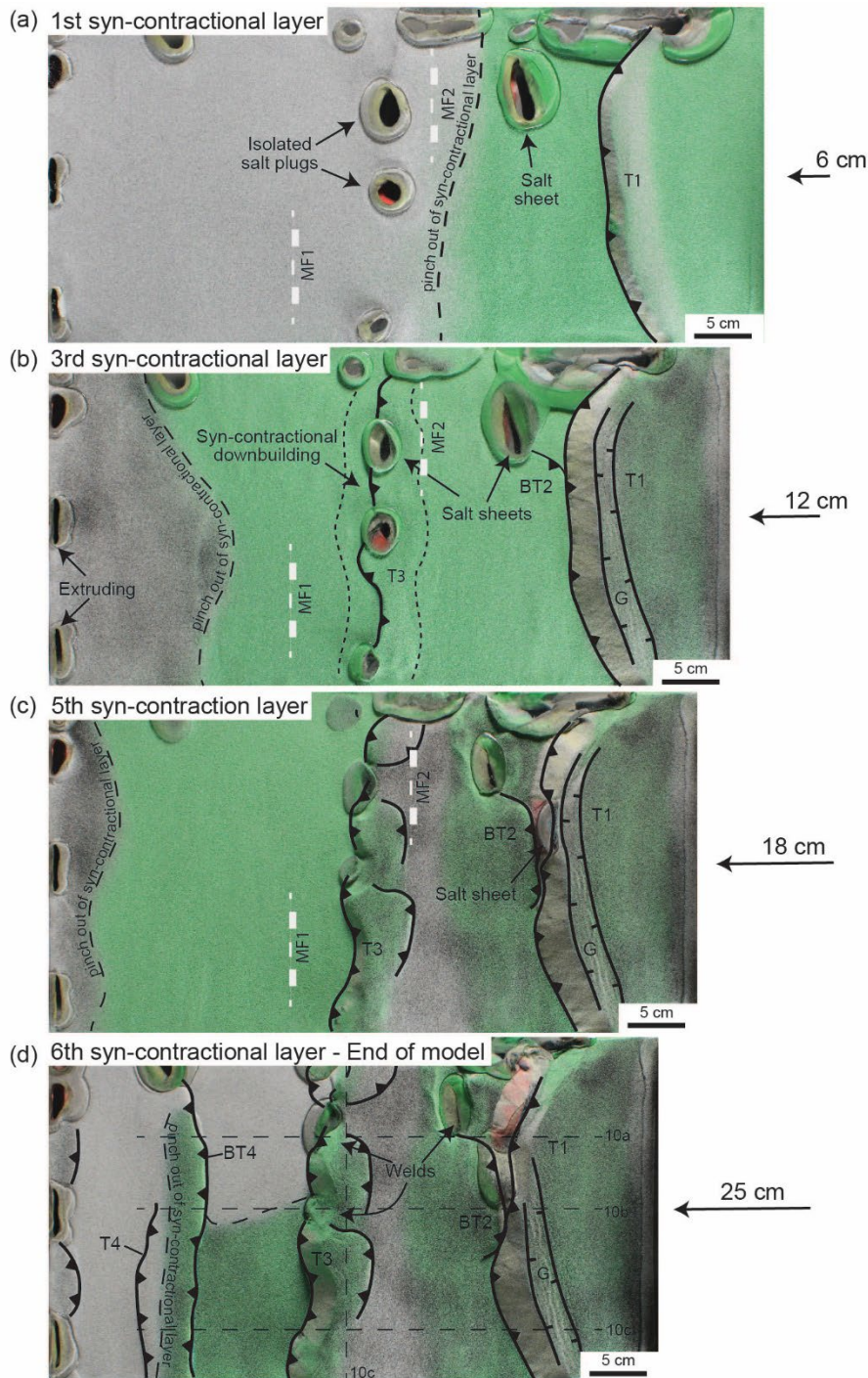
Figure 11. Top-view images illustrating the contractional kinematic evolution of Model 3, including the timing of thrust initiation, model salt extrusion from salt sheets, contractional welding of salt sheets, and the distribution of syn-contractional sedimentation. Abbreviations: T – thrust, G – graben, BT – back thrust, P – pop-up structure.
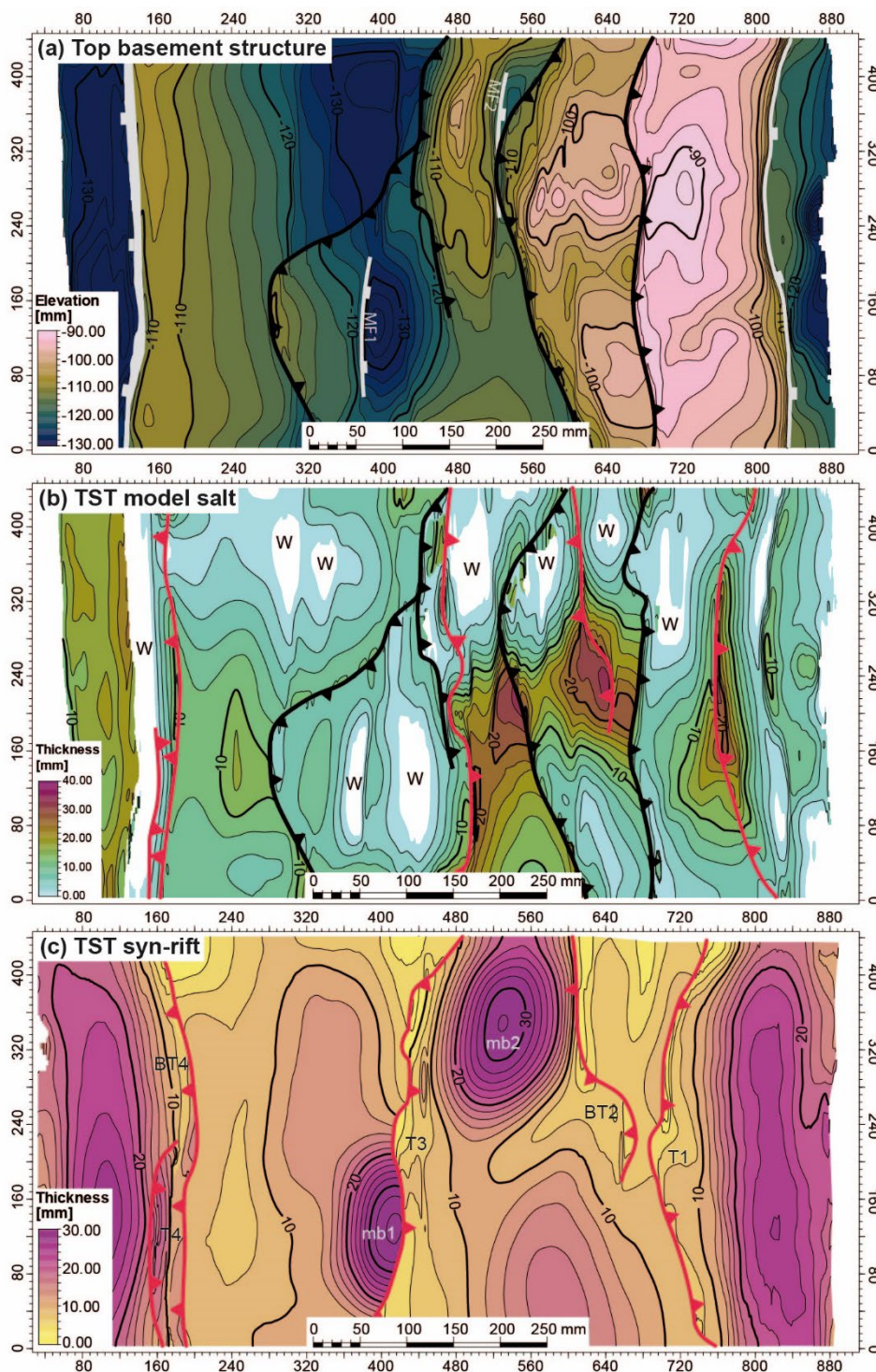
Figure 12. Structure and true stratigraphic thickness (TST) maps of key horizons in Model 3: (a) Top basement structure map of Model 2, (b) TST syn-rift map, and (c) TST autochthonous salt map. Basement thrusts are in black and cover thrusts are in red.

470 significant syn-contractional model salt extrusion (Figs. 11, 12b) and with the areas of highest elevation along the basement thrust sheets in the hinterland (Figs. 12a, 12b). Like Model 2, the basement thrusts leave clear imprints on the final model salt distribution and the thrust fronts can easily be interpreted across the thickness map. The cover thrust system leaves a less obvious influence on the final model salt distribution. Salt anticlines and salt walls appear as steep-sided structures in the model salt TST map, below the cover thrusts (Fig. 12b). The largest amount of preserved model salt across the basement

475 transfer zone occurs below the hanging wall of T3 (Figs. 10a-b, 12b).

The TST map of the syn-rift succession reveals the location of the syn-rift depocenters and their location in relation to the cover thrust system (Fig. 12c). Unlike Model 2, the depocenters do not consistently remain in the footwalls of the thrust sheets. The left-hand (foreland) marginal minibasin forms the hanging wall of BT4. However, no thrust develops ahead (forelandward) of mb1 and, therefore, mb1 remains in the footwall of T3 at the end of the model. As in Model 2, the thinnest part of the syn-

480 rift succession is adjacent to the interpreted thrust fronts of each of the faults in the cover thrust system (Fig. 12c).

4. Discussion

In the following section, we analyze the influence of salt in the formation and inversion of laterally segmented salt-bearing rift basins. Our analogue models are then compared to natural examples of salt-bearing rift basins inverted to different degrees, namely the northern Lusitanian Basin of Portugal and the Southern Pyrenees of Spain.

485 **4.1 Extensional deformation and syn-rift sedimentation in salt-bearing segmented rifts**

In our models, the syn-rift basin geometry and related sediment distribution are strongly controlled by the position of the underlying pre-salt basement faults, the amount and rate of slip attained by those faults, the original distribution and thickness of model salt, as well as the thickness and mechanical properties of the pre-kinematic sand pack (e.g., Withjack et al., 1990, Withjack and Callaway, 2000; Ferrer et al., 2014, 2016, 2022; Tavani and Granado, 2015; Roma et al., 2018a; Granado et al.

490 2021). In our models, syn-rift faults nucleated over velocity discontinuities imposed by the experimental set-up: at the lateral basal polymer pinch-outs, at the transition points between the three basal materials, and at the edge of the silicone seeds that controlled the location of the major faults (Fig. 2). The triangular section of the silicone seeds constrained the nucleation of listric master faults (i.e., MF1 and MF2), whereas smaller planar extensional faults develop along the other velocity discontinuities. The metal plate contact forms a more effective discontinuity, and extensional faults with greater offset than

495 those faults that nucleate along the rubber- and mylar-sheet contacts. The relatively greater offset created by the thickness of the metal plate compared to the thinness of the mylar sheet may thus relate to differences in fault nucleation effectiveness. In our models, the large syn-rift extensional faults grew by the lateral propagation of their tips, in a rather similar fashion to natural systems (e.g., Peacock and Sanderson, 1991; Cartwright et al., 1995), whereas across the transfer zone in between, a more diffuse fault array develops and forms a horst in cross section (Fig. 4b). However, this horst structure forms a saddle in

500 map view with a lower elevation than the adjacent basement along strike (Fig. 6a). The results of our modelling program highlight two key points: the relative timing of fault activity and the intervening phases of syn-rift sedimentation have a strong impact on the geometry of syn-rift basins, and that the thick (i.e., 1cm minimum) layer of syn-rift salt deposited after Phase 1 of extension favored the complete decoupling of extensional deformation between the pre- and the post-salt extensional systems. As a result, two very different extensional deformation styles developed. Similar results have been obtained in

505 analogue models by Dooley et al. (2003), Vendeville et al. (1995), Withjack et al. (1990), and Withjack & Callaway (2000). The model salt and cover sequence accommodate basement extension via stretching and thinning. The interplay between basement extension and syn-rift sedimentary loading initiate salt migration from the basement lows towards the margins of the sedimentary depocenters, as observed as well in previous works (e.g., Ferrer et al., 2014; Granado et al. 2021; Hudec & Jackson, 2007; Kehle, 1988; Koyi et al., 1993; Roma et al., 2018a). This creates a positive feedback loop that accelerates the
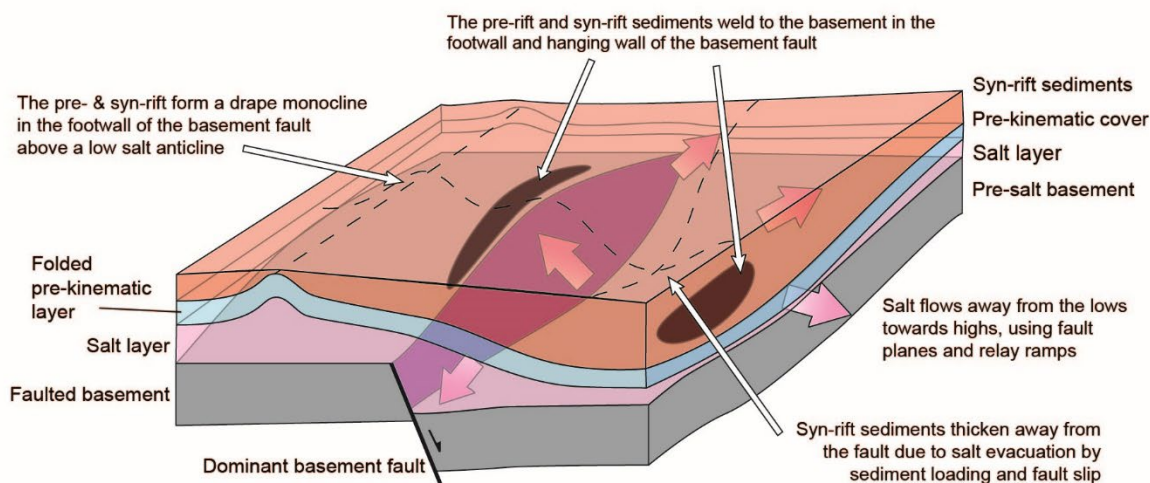
510

Figure 13. Block diagram illustrating the structural style of decoupled extensional rift half-graben with thick early syn-rift salt and a thin pre-kinematic layer bed showing the migration and inflation of salt away from the half-graben and the development of a synclinal minibasin within the basement half-graben. Modified and updated from Richardson et al (2005).

migration of salt from the basement lows as the subsiding minibasins thicken and sink deeper (e.g., Santolaria et al. 2021a).
515   However, the dimensions and location of the depocenters for mb1 and mb2 do not reflect the underlying basement geometries. In cross- and strike-sections, the syn-rift minibasins have symmetrical synclinal geometries that hamper the interpretation of the location and polarity of the underlying basement faults (Fig. 4), and thus contradict the structural dogma of the relationship between fault geometry and that of its hanging wall layers (i.e., White et al. 1986). The margins of the minibasins extend beyond the underlying downthrown basement blocks, masking the locations of the normal faults (Figs. 4a, c; 6b). Without
520   prior knowledge of the basement tectonic history, it would be very difficult to link the kinematic evolution of the cover depocenters to the underlying basement extensional system. Yet the depocenters of the syn-rift minibasins develop adjacent to the underlying basement faults and their locations still correlate with the displacement maxima of the hanging wall block (Figs. 4a, c; compare Fig.1 and Fig.13). The thickness map of the syn-rift succession highlights that the areas of thinner stratigraphy correspond with areas of underlying model salt inflation in the form of pillows, anticlines, and salt walls across the transfer
525   zone, while areas of non-deposition/erosion correspond with locations where inflated salt has pierced the cover sequence and spread over the model surface (Fig. 5). These results are important for the interpretation of seismic data, and the location of wells in pre-salt targets. In our models, areas of salt inflation are found over the footwall blocks away from the underlying basement faults (e.g., Koyi et al., 1993; Withjack & Callaway, 2000; Granado et al., 2021), but also along the transfer zone as an elongate, slightly sinuous salt anticline crossing from the hanging wall of MF1 to the footwall of MF2. In this salt ridge
530   across the transfer zone, the thickest salt accumulation corresponds to the salt wall over the hanging wall of MF1. Remnant salt is trapped against the fault planes of the master faults and the overlying hanging wall cover succession (Figs. 4a-c and 13).

Based on the results of our experimental program, we have updated the 3D block diagram from Richardson et al. (2005) to summarize the key salt structures, cover depocenters, and other features related to the interplay between basement extension, salt migration, and syn-rift sedimentation (Figs. 1 and 13). The model proposed by Richardson et al. (2005) includes a
535   comparatively thicker pre-kinematic layer than that used in our analogue models. A thinner pre-kinematic layer facilitates the development of shorter wavelength and higher amplitude forced fold across the basement fault, as shown in earlier works (e.g., Withjack, and Callaway, 2000). One relevant implication is the lateral boundaries of hanging wall minibasins, and the distribution of the syn-rift sedimentary infill: minibasins with high-amplitude and short wavelength force-folded pre-kinematic layers would favor the vertical aggradation of downbuilt syn-rift sediments, while longer wavelength and shorter amplitude
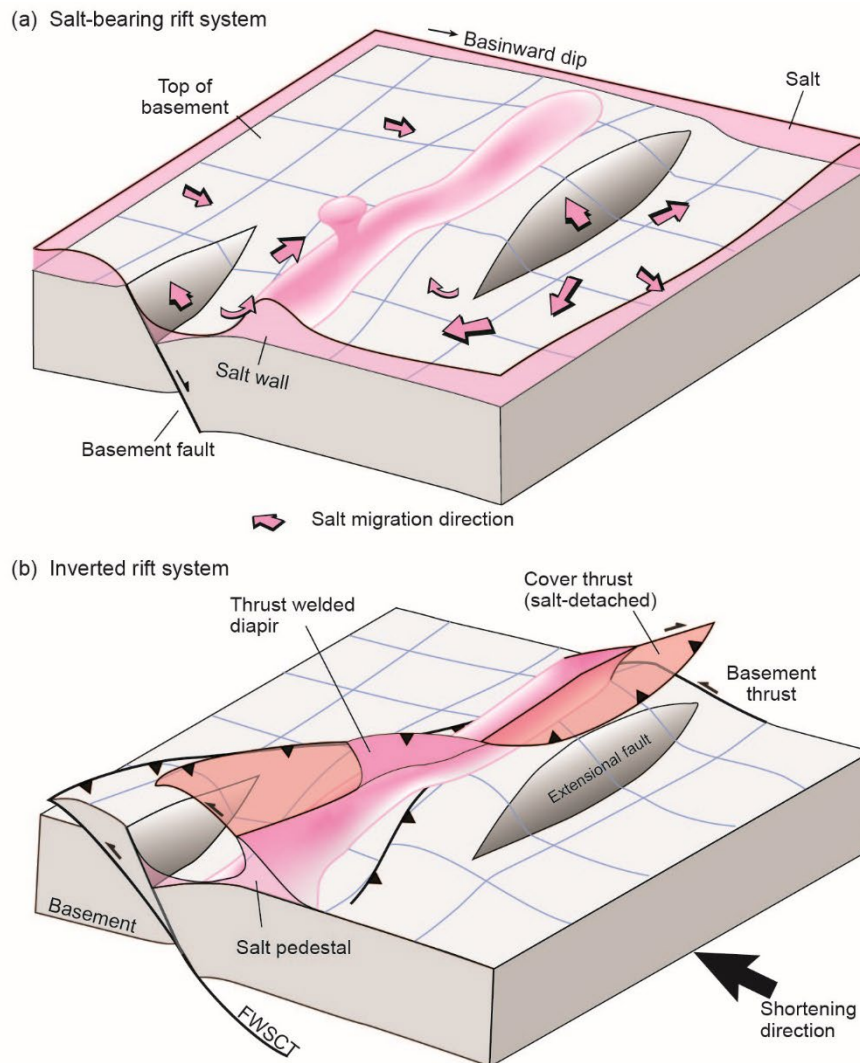
540

Figure 14. 3D schematic block diagrams illustrating the relationship between basement fault extension and the migration of salt caused by extension and downbuilding of cover strata (a), and how the salt interacts with the underlying basement thrust system and controls the location of thrusts through the cover sequence during subsequent shortening (b).

force-folded layers should favor the lateral expansion of syn-rift sediments. This model also shows that the syn-rift depocenter
545   is shifted away from the basement fault. The model by Richardson et al. (2005) shows a forced fold with four-way dip closures on the footwall of isolated basement faults; syn-rift layers onlap the periclinal termination of these footwall anticlines, resulting in a syn-rift sediment pinch-out with a concave to the fault arcuate geometry (Fig. 1). Conversely, our models show a continuous salt ridge stretching from the hanging wall of MF1 to the footwall of MF2 across the transfer zone (Fig. 15a), precluding the formation of an isolated four-way dip closure anticline on the footwall of MF2. This results in different syn-rift
550   pinch-out geometries, which are rather elliptical in plan-view (Fig. 6b). Mb1, however, fits better with the model proposed by Richardson et al. (2005), since its footwall has not interacted with any other fault (due to the model set up limitations). A diapir formed along transfer zone by a combination of stretching of the overburden and erosional piercement atop inflated salt. This is evidenced by the unconformity between pre-kinematic and syn-kinematic layers at both flanks of the structure (Fig. 4c). A

salt sheet extruding towards subsiding mb1 formed during the end of rifting (Fig. 5c) and grew passively during the deposition
555 of the post-rift sand pack (Fig. 4c). Extrusion of model salt was probably enhanced by the impinging of the overburden above
the footwall of MF1 forming a primary weld, as Stewart (2017) and Ferrer et al. (2022) have pointed out in previous works.
The occurrence of these large salt walls and local salt extrusion across transfer zones have also important implications for the
subsequent shortening phases, and in particular, for the orientation of contractional structures in respect to the regional direction
of shortening.

4.2 Influence of salt and syn-contractional sedimentation on contractional structural styles and kinematics

560

In our models 2 and 3, thick syn-rift model salt and associated structures, and the presence of syn-contractional sedimentation
played key roles in the structural styles and kinematics of the contractional fault systems. In both models, thick syn-rift model
salt controls the structural style of the cover thrust system and transfer of contractional deformation ahead of the moving
backstop wall. Syn-contractional sedimentation is added as an additional controlling factor in Model 3. In this way, Model 2
565 can be used as a control model for contractional deformation to differentiate the effects of the model salt décollement on
structural style and thrust kinematics from those imposed by syn-contractional sedimentation.

Both models have a generally foreland propagating thrust style in the basement and cover systems. As during extension, the
model salt decoupled the basement and cover thrust systems for the duration of contraction, except in locations of primary
welding. In those positions, however, the thrust systems did not link via faulting. Comparison of TST model salt maps for
570 models 1-3 (Figs. 6b, 9b, 12b) suggest that additional primary welds developed during shortening, attributed to basement thrust
uplift and propagation, as well as syn-contraction model salt extrusion. Reactivation of the main extensional faults during
shortening has been achieved by the nucleation of the basement thrusts in the silicone seeds. The other minor preexisting
extensional faults were not reactivated as thrusts, as is common in analogue models built using sand layers, the (e.g., Eisenstadt
and Simms, 2005; Ferrer et al., 2014; Granado et al. 2017). Instead, low-angle thrusts detached on the basal silicone layer,
575 crosscutting the preexisting extensional fault system (Figs. 7, 10).

As proven by previous studies, areas of inflated salt (e.g., salt anticlines, walls, and plugs) absorb and nucleate contractional
deformation (e.g., Vendeville et al., 1993; Vendeville and Nilsen, 1995; Letouzey et al., 1995; Brun and Fort, 2004; Rowan
and Vendeville, 2006; Hudec and Jackson, 2007; Dooley et al., 2009; Duffy et al., 2018; Roma et al., 2018a; Granado et al.,
2021; Santolaria et al., 2021a, b; 2022). In our models, this process began since early stages of shortening, as evidenced by
580 narrowing of salt diapirs (Figs. 8, 11, and Supplemental Material). Our results indicate that the geometry of salt diapirs and
salt structures dictates the nucleation of thrusts, and strongly influences the subsequent thrust kinematics. Diapirs preferentially
developed in the transfer zone between the two major extensional faults and along the salt ridges. They record the onset of
shortening in the foreland away from the thrust front and determined the linkage of the thrusts reactivating the major
extensional faults as contractional deformation progressed forward (Figs. 8 and 11). In model 2 with no syntectonic
585 sedimentation the squeezed diapir of the transfer zone linked with the back thrust related to the reactivation of MF2 and the
thrust squeezing the salt structure in the hanging wall of the reactivated MF1. As a result, the change of vergence and the
oblique structures connecting with the welded diapir revealed the existence of a former transfer zone in the basement faults,
regardless of the decoupling between the basement and the post-salt succession. In Model 3, syntectonic sedimentation in the
footwall of the reactivated MF2 prevented the development of the back thrust in front of mb2, resulting in a more linear
590 structure and masking the existence of the transfer zone (Figs. 10a and 11). This linearity has been enhanced by the along
strike coincidence of the salt anticline above the rollover anticline in the hanging wall of MF1 and the salt anticline in the
footwall of MF2, regardless the saddle between both anticlines coinciding with the transfer zone (Figs. 4, 5 and 11). Random
thrust vergence (i.e., fore-thrusts *vs.* back-thrusts) is one characteristic behavior of thrust wedges formed on non-frictional
décollements (e.g., Davis and Engelder, 1985; Costa and Vendeville, 2002). However, several factors in our models may have
595 also favored the development of oppositely verging thrusts, particularly for those structures showing a sudden change in
vergence along strike (i.e., Model 2), including: the location of primary welds relative to the squeezed salt wall, the distribution
of the cover sequence both across and along the salt wall, and the width of the salt wall. The thickness of the original model

salt, and by extension, the thickness of the cover sequence, seem to be one controlling factor as the thick minibasins tend to
remain on a footwall position (Fig. 7). This is much contrary to what is expected to happen upon basin inversion. Isolated sub-
600   circular plugs nucleate foreland-propagating thrusts that tend to link up if other thrusts initiate along strike, in the same
structural position (Figs. 11b-d). It has been proven in many experimental programs that the geometry and the position of
emergent thrusts is strongly influenced by erosion and sedimentation processes (e.g., Storti and McClay, 1995; Mugnier et al.
1997; Graveleau et al. 2012). Conversely, recent works propose that the location and distribution of the early salt structures
and related syn-rift minibasins, determine the location, wavelength, and vergence of thrusts in the cover system, regardless of
605   the presence of syn-contractional sedimentation (e.g., Roma et al., 2018a; Dooley and Hudec, 2020; Santolaria et al. 2021a,
b). In our models, however, the difference in the pattern of thrust vergence without (Model 2) and with syn-contractional
sedimentation (Model 3) is striking. It is also remarkable that both models show significant differences on the geometries of
basement thrusting, and the associated distribution of structural relief, and thrust sequence. These differences evidence the role
imposed by syn-contractional sedimentation in controlling the large-scale kinematics of thrust wedges (i.e., cover and
610   basement), since the presence of early salt structures and syn-rift minibasins is broadly equal on both models. In our models,
the location and geometry of the syn-rift salt structures reflect the inherited extensional basement fault array, which due to the
model set-up run broadly perpendicular to the direction of extension and shortening. However, the observed relationships have
been transported by thrusting: this is important to note because it could help reconstructing the pre-shortening configuration
of a rifted margin that has been detached its original position, or in areas where the sub-salt configuration is obscured. Note as
615   well that in such a case, the geometry of the syn-rift minibasin cannot not be used to infer the polarity of the basement fault
array (i.e., whether left- or right-dipping, in model coordinates).

Syn-contractional sedimentation was added to Model 3 as a prograding sedimentary wedge that onlapped the underlying cover
sequence. This sedimentary wedge triggered syn-contractional downbuilding, enhanced model salt extrusion due to salt
evacuation, and altered the rate of transference of contractional deformation from what was seen in Model 2. The syn-
620   contractional sedimentary wedge renewed downbuilding via differential loading. The syn-contractional were folded into
footwall synclines beneath emergent thrust fronts, forcing salt evacuation from below the footwalls, as well as enhancing salt
extrusion from preexisting salt structures by combining syn-contractional extrusion with downbuilding. Local areas of higher
model salt extrusion are reflected by the uneven thicknesses and distribution of the syn-contractional sedimentation across
Model 3 (compare Figs. 7a and 7c; Fig. 11), and the TST map of the model salt (Fig. 12c).

625   The missing model salt in the hanging wall of the cover thrusts proximal to the thrust fronts in Model 2 could also be related
to the difference in the rate of transference of contractional deformation into the foreland between models 2 and 3. There is a
difference in the thrust sequencing in cover thrust systems between models 2 and 3. There is a delay in the propagation of
thrusts towards the foreland with syn-contractional deformation. In addition, more back thrusts developed with no syn-
contractional sedimentation (Figs.7, 8, 15a; see Supplemental Material). The out of sequence thrust system in Model 2 indicates
630   that deformation was transferred rapidly across the model, utilizing any and all weak points to nucleate thrusts (Fig. 14a). None
of these structural features are seen in Model 3. In fact, the timing of thrust nucleation in the cover system has a relatively
linear relationship with time (Fig. 14b). We attribute this change in thrust nucleation timing with the addition of syn-
contractional sediment at regular intervals. The syn-contractional sedimentary wedge changed the taper angle of the thrust
wedge, focusing deformation in the hinterland until critical taper was once again attained, allowing contractional deformation
635   to propagate farther into the foreland.
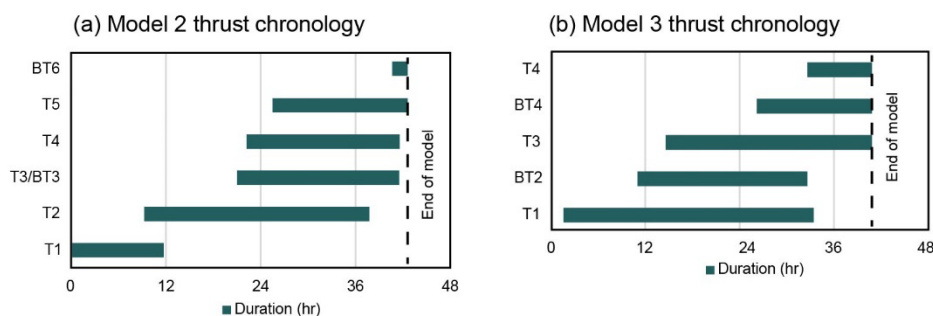
Figure 15. Graphs illustrating the timing of initiation and duration of each contractional feature for Model 2 (a) and Model 3 (b). The timing of thrusts in Model 3 has a more linear relationship than those of Model 2, which has an exponential curved shape.

Based on the results of the shortened models, we propose a model illustrated by 3D block diagram showing the inversion of a salt-bearing segmented rift (Fig. 14b). During shortening, the salt inflated areas localize shortening via squeezing and as décollements for thrusts in the cover (Fig. 14b). Extrusive salt diapirs localize thrust fronts while elongated salt walls nucleate thrusts with opposing vergence, regardless of the presence of syn-contractional sedimentation. Inversion of the basement system results in the preferential development of footwall shortcuts across preexisting extensional faults. Individual thrusts may join by segment linkage to form oblique ramps across extensional transfer zones.

4.3 Insights for natural systems

The results of analogue models of an inverted segmented rift system with early syn-rift salt are compared with natural examples from the northern Lusitanian Basin in offshore Portugal and the South-Central Pyrenean fold and thrust belt in Spain (Fig. 16). The three natural case studies show increasing amounts of inversion and shortening, from very little in the northern Lusitanian basin, to full basin inversion and incorporation in the thrust system in the Southern Pyrenees case.

4.3.1 Northern Lusitanian Basin, offshore Portugal

The northern Lusitanian Basin offshore Portugal records several multirift events, from Late Triassic to Early Cretaceous, related to the opening of the North Atlantic (e.g., Alves et al., 2002; Rasmussen et al., 1998; Stapel et al., 1996). The northern Lusitanian basin is also mildly inverted as a result of the Alpine orogeny, with a relatively minor Eocene compression event followed by a more pronounced period of Miocene deformation, characterized by folding, minor faulting and erosion (e.g., Pinheiro et al., 1996; Ribeiro et al. 1990). According to these authors, the Dagorda salt of the northern Lusitanian basin was deposited during Triassic rifting, pointing out the occurrence of salt migration during the Triassic, Jurassic and the Early Cretaceous rift events. In the salt-prone regions of the basin, broad minibasins developed above the hanging wall blocks of pre-salt basement faults, forcing salt to inflate on the footwall blocks of basement faults (see Alves et al., 2002; Fig. 16a), probably aided by differential sediment loading. Thus, the northern Lusitanian basin is comparable to our analogue models since the origin of salt structures can be related to the interaction of pre-salt basement fault kinematics and syn-rift sedimentation in the presence of thick syn-rift salt.

In the interpreted seismic profile (Fig. 16a), the cover sequence is characterized by a broad salt-withdrawal minibasin affected by several salt-detached folds above an uneven basement. Salt-detached cover folds are located at the edges of the main syn-rift depocenter, while a larger anticline is observed in the middle of the seismic profile. The syn-rift sequence is characterized by a series of reflectors that apparently downlap on the pre-kinematic series towards the SW of the profile, while the same reflectors onlap on the pre-kinematic units towards the NE end of the seismic line. These reflector terminations are broadly similar to those produced in our sandbox models and are indicative of extension by underlying faults while sediment loads and
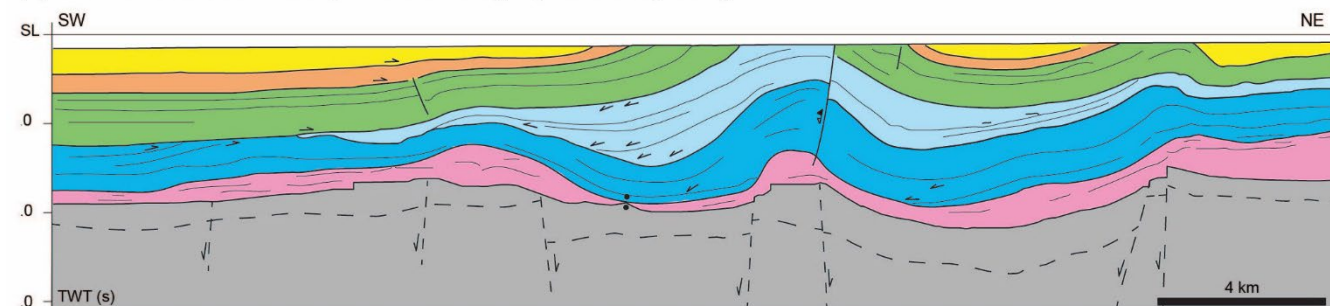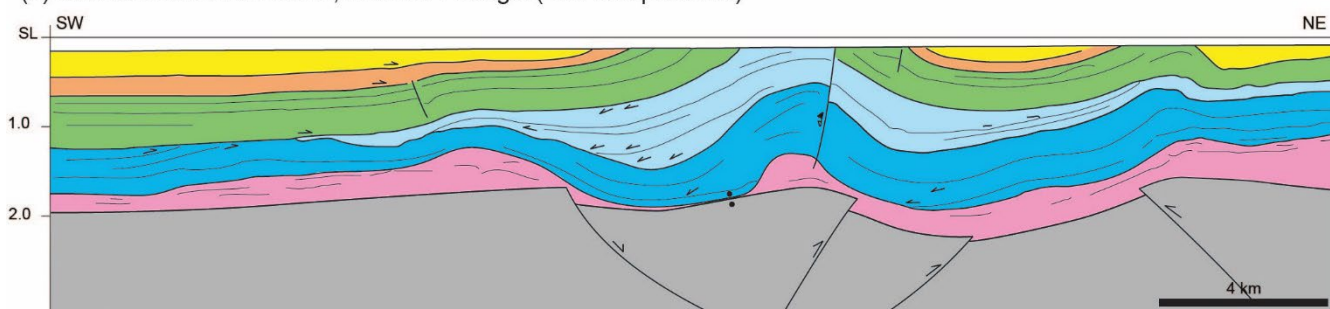
Figure 16. Line drawings of seismic sections showing variable degrees of inversion of salt-detached extensional systems. (a) Interpreted seismic line S84-23 of the northern Lusitanian Basin (offshore Portugal) (modified from Alves et al., 2002); (b) New interpretation of the basement of seismic line S84-23. Abbreviations: Tr: Triassic, Jr: Jurassic; K: Cretaceous; L: Lower; U: Upper.

evacuates underlying salt. The apparent downlap most probably results from the folding and inversion of previous onlap geometries, as also shown by previous authors in other salt-bearing rift basins (e.g., Tavani and Granado, 2015) and numerical models (e.g., Granado et al. 2021).

While there is good enough imaging to define the base salt in this section of the northern Lusitanian Basin, it leaves the structural style of the basement open to question. Differing interpretations have been provided to explain the observed geometries of the inverted post-salt extensional basins. For instance, Alves et al. (2002) originally interpreted these syn-rift basins as salt withdrawal minibasins mostly inverted by thin-skinned shortening, with the evaporites acting as a regionally decoupling horizon. The implications from such interpretation, as shown by our models, is that if pure thin-skinned shortening has taken place, the pre-salt basement faults responsible for crustal thinning and syn-rift accommodation space may not be directly below the salt structures and related cover folds. The salt structures and related depocenters may have been transported along the decoupling horizon, and thus laterally shifted from the underlying basement fault array. Alternatively, Roma et al. (2018b) interpreted the individual syn-rift basin as salt-detached ramp syncline basin, whose tectonic inversion was accomplished by the reactivation of an underlying basement fault with a ramp-flat-ramp geometry. The sections of our models (Figs. 7, 10) may provide a glimpse towards a more evolved and inverted equivalent to the northern Lusitanian basin. However, certain improvements can be made in the interpretation of the seismic profile based on our models: the presence of basal primary welds, not originally interpreted by previous authors (i.e., Alves et al., 2002, their Fig. 10; our Fig. 16a), for instance. The uplift and basinward (SW) rotation of the syn-rift depocenter in the central portion of the profile could be attributed to salt squeezing, mild inversion of a normal fault in the cover sequence (Alves et al., 2002), the mild inversion of preexisting normal

690 faults and, most likely some combination of the two as can be seen in our models. Taking these concepts from the results of our models, the pre-salt basement in the seismic profile could be reinterpreted to show a primary welded syn-rift basin above reactivated basement faults (Fig. 16b).

4.3.2 Isàbena area, South-Central Pyrenees, Spain

The Pyrenean orogen formed during the Late Cretaceous to Miocene collision of the Iberian and European plates (Muñoz et
695 al., 2018 and sources therein). The South-Central Pyrenean fold-and-thrust belt is part of the southern thrust system of the doubly verging Pyrenean orogen. It is characterized by the inversion of the Late Jurassic-Early Cretaceous salt-bearing segmented rift system developed along the North Iberian Margin (Tugend et al., 2014; Tavani et al. 2018). The fold-and-thrust belt is characterized by a series of thrust sheets that involved a Mesozoic succession decoupled it from its autochthonous basement along the Triassic evaporites (Fig. 17). Available seismic lines and tied exploration wells allowed for a constrained
700 interpretation of key structural features of the fold-and-thrust belt beyond extensive surface data (Muñoz, 1992; Muñoz et al., 2018). Unlike the previous two examples, the South-Central Pyrenees are an example of a fold-and-thrust belt that has
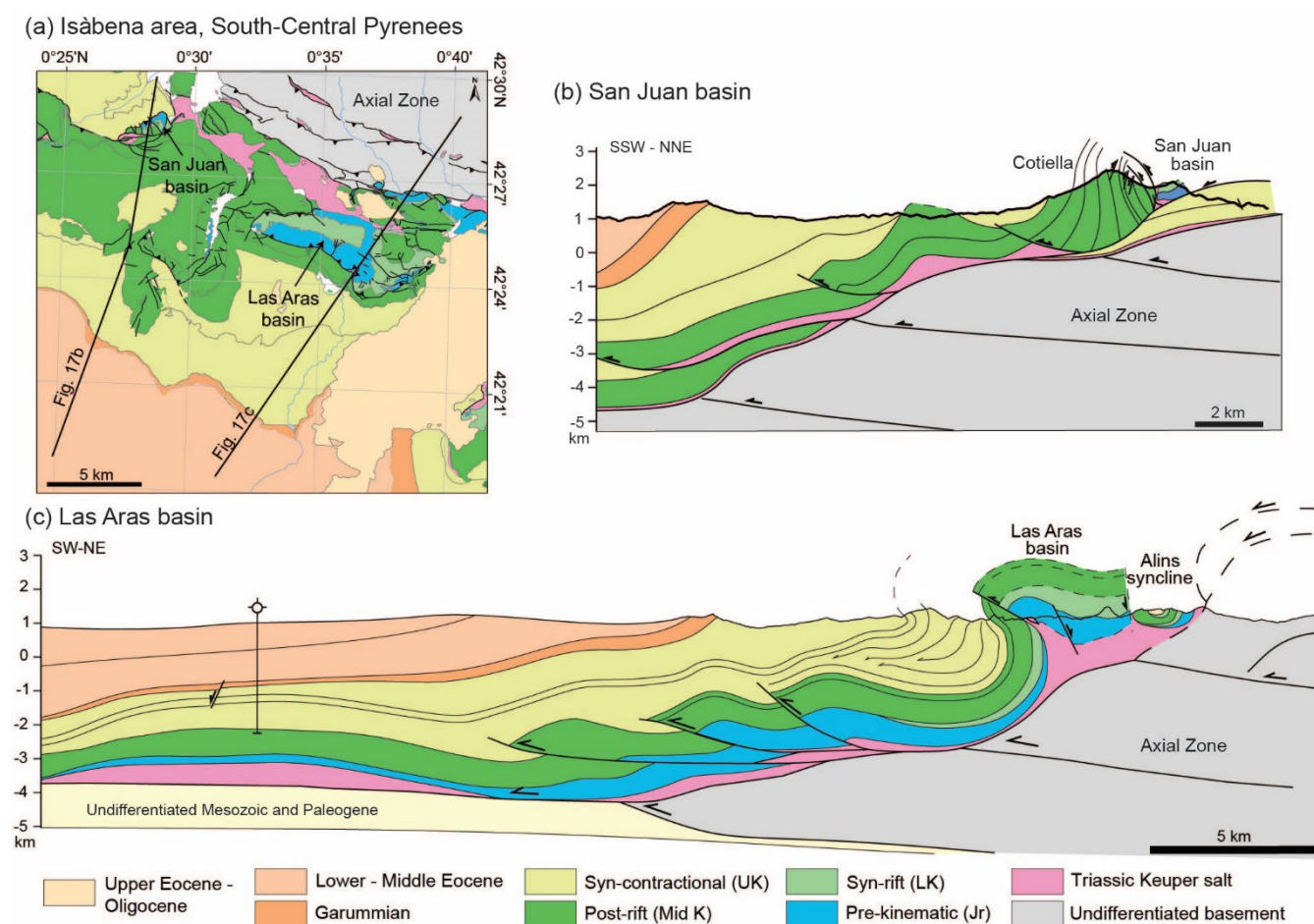
Figure 17. (a) Map showing the location of cross-sections through the San Juan and Las Aras basins, South-Central Pyrenees (compiled from Robador and Zamorano, 1999; García-Senz and Ramírez, 1997). (b) Cross-section through the San Juan basin. (c)
705 Transect across the Las Aras basin (modified from Muñoz et al., 2018). Abbreviations: Jr: Jurassic; K: Cretaceous; L: Lower; U: Upper.

undergone more inversion and shortening than our analogue models as the rift system has been completed detached and transported from its original position and can no longer be correlated to the underlying basement structures responsible for crustal thinning.

710   Several examples of inverted syn-rift basins have been interpreted in the South-Central Pyrenees, including the Organyà, Aulet, and Las Aras basins (Muñoz, 1992; Garcia-Senz, 2002). We have selected the Isàbena area to illustrate key similarities in the geometries of structures within the Pyrenean example and our models (Fig. 17). Two syn-rift basins (i.e., Las Aras and San Juan basins) have been inverted and transported in a salt-detached thrust system while apparently maintaining their original segmented configuration (Fig. 17a). The zone between the two syn-rift basins is defined by the development of a large post-
715   rift basin (the Cotiella basin system) and a series of oblique salt-detached anticlines, flanked by growth synclines filled by syn-contractional turbidites (e.g., Garcia-Senz, 2002; Ramos et al., 2020). Very little of the San Juan basin is preserved as a result of erosion, but some salt is preserved in the contact with the Cotiella basin to the SW, which can be interpreted as a squeezed diapir that developed in the footwall of a former extensional fault (Fig. 17b). The Las Aras basin is characterized by an anticline along the basin's southwestern margin. To the north, Aptian syn-rift strata are onlapping previously eroded Jurassic
720   dolostones (Garcia-Senz, 2002) thus suggesting that the Jurassic strata were forced folded upon rifting, favored by the decoupling of the Triassic evaporites. To the NE, the Las Aras basin is secondary welded to the Alins syncline, so it is likely that interaction with a growing salt diapir along the northern margin of the basin controlled the deposition of the syn-rift succession.

Salt tectonics continued to influence the system into the post-rift. The post-rift succession is fairly uniform across the section
725   through Las Aras (Fig. 17c). However, in the section through the San Juan basin, and to the W, the Cotiella Massif developed as post-rift gravity driven extensional basins (López-Mir et al., 2015). The cover system has been transported some tens of kilometers from its original position, so it is difficult to determine the degree of coupling between the cover syn-rift basins and underlying basement extensional fault array. However, based on comparison with our analogue models, we can infer that the basement master faults and associated half-grabens (or grabens) were located beneath the Las Aras and San Juan basins. And
730   assuming that the system has been transported in such a way to maintain their original relational positions, the two syn-rift basins were separated by a wide transfer zone. Today, the transfer zone is characterized by a tight, obliquely oriented salt-cored anticline, flanked by syn-contractional sediments.

The rate and amount of syn-contractional sedimentation is much higher in this Pyrenean example than in our models. Similar to our models, the syn-contractional sedimentation flanking the inverted syn-rift basins constrains the timing of inversion and
735   thrust initiation, especially in the section through Las Aras, where apparent seismic reflectors onlap the buried Triassic salt-detached thrust sheet (Fig. 17c). The thickness of the syn-contractional succession is sufficient to support the inversion, uplift, and folding of the Las Aras basin in the hanging wall of the Las Aras thrust, and syn-contractional footwall synclines develop. Section across the Las Aras basin shows some similarities to the section across mb2 in our model 3 with syn-contractional deformation (Figs. 10a and 17c) suggesting us ideas for the interpretation of the basement sub-salt geometries. One of the
740   problems for the interpretation of the Las Aras section is the structural difference between the bottom of the synorogenic basin in the footwall of the inverted syn-rift basin and its equivalent above the syn-rift depocenter. Such several km high structural relief is interpreted as the result of basement underthrusting, but the problem is the restored geometry at the time of synorogenic sedimentation considering the decoupling between the cover and the basement. The accommodation space for the thick synorogenic depocenter will be partially resulted from the salt evacuation of a previously salt inflated area south of the Las
745   Aras depocenter, in the footwall of a basement-involved extensional fault. The overturned limb of the footwall syncline would have developed above the short-cut of the extensional fault and the basement could have been welded underneath the syn-rift depocenter limiting the amount of decoupling. Nevertheless, such decoupling between cover and basement would occur further to the north and south and the degree of relative displacement between the cover and the basement along the Triassic salt would not be constant (Figs. 10 and 17).

750   In the South-Central Pyrenees, unlike our models, basement involved shortening has interpreted to occur after the development of the cover thrust system and is recorded by squeezing of pre-existing folds (Figs. 17b, c). However, model results and the previous discussion above challenge this interpretation. In any case, in both the Pyrenees and our models, the basement thrust system is responsible for the regional uplift and geometry of the thrust wedge (Figs. 7a-c, 10a-c. 17), and the intervening salt layer keeps the cover thrust systems decoupled.

755   **Conclusions**

The results of the analogue modelling program presented in this paper provide geometric and kinematic insights of contractional systems that involve the inversion of extensional basins with thick syn-rift salt. The extensional basement fault system controlled the location of overlying syn-rift depocenters and the evacuation pathways and inflation areas for the syn-rift salt layer. Synclinal minibasins developed above the hanging walls of the extensional basement faults (Fig. 4) forcing salt
760   to migrate away from the downbuilding basins. The salt flowed along fault planes and dipping basement panels updip into basement highs to form salt structures in the basement footwall blocks, in the hanging wall block along the margins of the syn-rift minibasins, and across the transfer zone (Fig. 15a). Typical salt structures that develop are reactive to passive salt diapirs and salt anticlines which are generally perpendicular to the direction of extension; diapiric salt walls and salt plugs can pierce the cover sequence where significant extension and syn-extensional erosion thin the overburden (Fig. 4c). The salt structure
765   across the transfer zone tends to link the hanging wall salt anticline of one extensional fault to the footwall salt anticline of the adjacent fault via an oblique salt anticline (Figs. 4b, 6c). The synclinal minibasins extend beyond the confines of the basement half-grabens, obscuring the geometry of the underlying basement fault array. Primary welding of the minibasins occurs in the footwall and hanging wall, but not necessarily under the minibasins thickness maximum.

Upon shortening, the syn-rift salt kept the basement and cover thrust systems decoupled and exerted a fundamental control
770   during inversion. The basement thrust system is characterized by low-angle thrusts and reactivation of the major extensional faults (Fig. 15b). An oblique ramp develops in the basement across the transfer zone. The cover thrust system is characterized by source-fed thrusts that nucleate on preexisting salt structures, including primary welds that reactivate as thrust welds. The salt structures experience squeezing early and nucleate thrusts and folds. The addition of syn-contractional sedimentation plays a key role in the propagation of deformation by delaying the transference of deformation into the foreland and possibly
775   imposing the vergence of thrusts only towards the foreland. Syn-contractional sedimentation also increases the rate of salt extrusion from preexisting diapirs and pierced thrust tips.

The 3D implications of our results indicate the importance of the interaction of salt between individual basin systems in salt-bearing segmented rift systems. In extensional systems with sufficiently thick salt, the salt evacuation pathways from downbuilding and extending minibasins can interact and modify the expected salt structure geometry, creating a salt ridge
780   from the hanging wall of one extensional basin to the footwall of the adjacent basin via the transfer zone (Fig. 15a). If the system then undergoes inversion and shortening, the distribution of inflated salt may control the location and style of thrusting in the cover sequence (Fig. 15b). This 3D understanding may provide insight and better templates for analyzing the trap potential for geological storage of CO_2, and production of geothermal energy in extensional to inverted salt-bearing rift basins.

Acknowledgment

785   This is a contribution of the Institut de Recerca Geomodels from the Universitat de Barcelona. We acknowledge the support of the SABREM (PID2020-117598GB-I00) research project funded by MCIN/ AEI /10.13039/501100011033 and the GEODIGIT (TED2021-130602BI00) research projects funded by MCIN/AEI/10.13039/501100011033 and for the European Union "NextGenerationEU"/PRTR. We thank the financial support of OMV Exploration and Production through project FBG310629. Research by E. P. Wilson is supported by an AGUAR pre-doctoral grant (2020 FI SDUR) from the Generalitat

790 de Catalunya. The Scientific colour maps *batlow*, *buda*, and *hawaii* from Crameri (2018) are used in this study to prevent visual distortion of data and exclusion of color vision deficiencies readers (Crameri et al., 2020).

Supplementary material

Time-lapse video of extension for Model 1.

Time-lapse video of shortening for Model 2 (no surface processes).

795 Time-lapse video of shortening for Model 3 (including syn-contractional sedimentation).

References

Adam, J., Urai, J. L., Wieneke, B., Oncken, O., Pfeiffer, K., Kukowski, N., Lohrmann, J., Hoth, S., van der Zee, W., and Schmatz, J.: Shear localisation and strain distribution during tectonic faulting—new insights from granular-flow experiments and high-resolution optical image correlation techniques, J Struct Geol, 27, 283–301,
800 https://doi.org/10.1016/J.JSG.2004.08.008, 2005.

Ahlrichs, N., Hübscher, C., Noack, V., Schnabel, M., Damm, V., and Krawczyk, C. M.: Structural Evolution at the Northeast North German Basin Margin: From Initial Triassic Salt Movement to Late Cretaceous-Cenozoic Remobilization, Tectonics, 39, https://doi.org/10.1029/2019TC005927, 2020.

Alves, T. M., Gawthorpe, R. L., Hunt, D. W., and Monteiro, J. H.: Jurassic tectono-sedimentary evolution of the Northern
805 Lusitanian Basin (offshore Portugal), Mar Pet Geol, 19, 727–754, https://doi.org/10.1016/S0264-8172(02)00036-3, 2002.

Alves, T. M., Mattos, N. H., Newnes, S., and Goodall, S.: Analysis of a basement fault zone with geothermal potential in the Southern North Sea, Geothermics, 102, 102398, https://doi.org/10.1016/J.GEOTHERMICS.2022.102398, 2022.

Amilibia, A., McClay, K. R., Sàbat, F., Muñoz, J. A., and Roca, E.: Analogue modelling of inverted oblique rift systems, Geologica Acta, 3, 251–271, 2005.

810 Beauchamp, W.: Superposed folding resulting from inversion of a synrift accommodation zone, Atlas Mountains; Morocco, in: Thrust tectonics and hydrocarbon systems, edited by: McClay, K. R., American Association of Petroleum Geologists, 635–646, https://doi.org/10.1306/m82813c33, 2004.

Bonini, M.: Deformation patterns and structural vergence in brittle–ductile thrust wedges: An additional analogue modelling perspective, J Struct Geol, 29, 141–158, https://doi.org/10.1016/J.JSG.2006.06.012, 2007.

815 Bonini, M., Sani, F., and Antonielli, B.: Basin inversion and contractional reactivation of inherited normal faults: A review based on previous and new experimental models, Tectonophysics, 522–523, 55–88, https://doi.org/10.1016/j.tecto.2011.11.014, 2012.

Brun, J.P. and Nalpas, T.: Graben inversion in nature and experiment, Tectonics, 15, 677–687, 1996.

Brun, J.P. and Beslier, M. O.: Mantle exhumation at passive margins, Earth Planet. Sci. Lett., 142, 161–173, 1996.

820 Buchanan, P. G. and McClay, K. R.: Sandbox experiments of inverted listric and planar fault systems, Tectonophysics, 188, https://doi.org/10.1016/0040-1951(91)90317-L, 1991.

Buchanan, P. G. and McClay, K. R.: Experiments on basin inversion above reactivated domino faults, Mar Pet Geol, 9, https://doi.org/10.1016/0264-8172(92)90061-I, 1992.

Cartwright, J.A., Trudgill, B.D., Mansfield, C.S.: Fault growth by segment linkage: an explanation for scatter in maximum displacement and trace length data from the Canyonlands Grabens of SE Utah, Journal of Structural Geology, 17(9), 1319-1326, 1995.

Célini, N., Callot, J.P., Ringenbach, J.C., and Graham, R.: Jurassic salt tectonics in the SW sub-Alpine fold-and-thrust belt. Tectonics, 39, e2020TC006107. https://doi.org/10.1029/2020TC006107, 2020.

Chapple, W.: Mechanics of thin-skinned fold-and-thrust belts, Am Assoc Pet Geol Bull, 89, 1978.

Costa, E., and Vendeville, B.C.: Experimental insights on the geometry and kinematics of fold-and-thrust belts above weak, viscous evaporitic décollement, Journal of Structural Geology, 24, 1729-1739, 2002

Coward, M. P.: Structural and tectonic setting of the Permo-Triassic basins of northwest Europe, Geol Soc Spec Publ, 91, https://doi.org/10.1144/GSL.SP.1995.091.01.02, 1995.

Crameri, F., Shephard, G. E., and Heron, P. J.: The misuse of colour in science communication, Nat Commun, 11, 5444, https://doi.org/10.1038/s41467-020-19160-7, 2020.

Crameri, F.: Geodynamic diagnostics, scientific visualisation and StagLab 3.0, Geosci Model Dev, 11, 2541–2562, https://doi.org/10.5194/GMD-11-2541-2018, 2018.

Davis, D.M., Engelder, T.: The role of salt in fold-and-thrust belts, Tectonophysics, 119, 67-88, 1985

Davy, P. and Cobbold, P. R.: Experiments on shortening of a 4-layer model of the continental lithosphere, Tectonophysics, 188, https://doi.org/10.1016/0040-1951(91)90311-F, 1991.

Dell'Ertole, D. and Schellart, W. P.: The development of sheath folds in viscously stratified materials in simple shear conditions: An analogue approach, J Struct Geol 56, https://doi.org/10.1016/j.jsg.2013.09.002, 2013.

Dooley, T., McClay, K. R., and Pascoe, R.: 3D analogue models of variable displacement extensional faults: Applications to the Revfallet Fault system, offshore mid-Norway, Geol Soc Spec Publ, 212, 151–167, https://doi.org/10.1144/GSL.SP.2003.212.01.10, 2003.

Dooley, T., McClay, K. R., Hempton, M., and Smit, D.: Salt tectonics above complex basement extensional fault systems: Results from analogue modelling, in: Petroleum Geology: North-West Europe and Global Perspectives - Proceedings of the 6th Petroleum Geology Conference, 1631–1648, https://doi.org/10.1144/0061631, 2005.

Dooley, T. P. and Hudec, M. R.: Extension and inversion of salt-bearing rift systems, Solid Earth, 11, 1187–1204, https://doi.org/10.5194/se-11-1187-2020, 2020.

Duffy, O. B., Dooley, T. P., Hudec, M. R., Jackson, M. P. A., Fernandez, N., Jackson, C. A. L., et al.: Structural evolution of salt-influenced fold-and-thrust belts: a synthesis and new insights from basins containing isolated salt diapirs. J. Struct. Geol. 114, 206–221. doi: 10.1016/j.jsg.2018.06.024, 2018

Duffy, O. B., Hudec, M. R., Peel, F., Apps, G., Bump, A., Moscardelli, L., Dooley, T. P., Bhattacharya, S., Wisian, K., and Shuster, M. W.: The Role of Salt Tectonics in the Energy Transition: An Overview and Future Challenges, https://doi.org/10.31223/X5363J, 2022.European Commission: Europe's 2030 climate and energy targets: Research & Innovation actions, European Commission, 2021.

Eisenstadt, G. and Sims, D.: Evaluating sand and clay models: Do rheological differences matter?, J Struct Geol, 27, 1399–1412, https://doi.org/10.1016/j.jsg.2005.04.010, 2005.

860 European Commission: Europe's 2030 climate and energy targets: Research & Innovation actions, European Commission, 2021.

Ferrer, O., Roca, E. & Vendeville, B. C.: The role of salt layers in the hangingwall deformation of kinked-planar extensional faults: insights from 3D analogue models and comparison with the Parentis Basin. Tectonophysics, 636, 338–350, 2014.

Ferrer, O., McClay, K., and Sellier, N. C.: Influence of fault geometries and mechanical anisotropies on the growth and
865 inversion of hanging-wall synclinal basins: Insights from sandbox models and natural examples, in: Geological Society Special Publication, vol. 439, https://doi.org/10.1144/SP439.8, 2016.

Ferrer, O., Carola, E.; McClay, K., Bufaliza, N.: Analog modeling of domino-style extensional basement fault systems with pre-kinematic salt. AAPG Bulletin, DOI:10.1306/08072221188, 2022.

Ferrer, O.; Carola, E.; McClay, K.: Structural control of inherited salt structures during inversion of a domino basement-fault
870 system from an analogue modelling approach. Solid Earth, submitted.

García-Senz, J.: Cuenca extensiva del cretácico inferior en los Pirineos centrales, formación y subsecuente inversión, 307 pp., 2002.

García-Senz, J., and Ramírez, I.: Mapa geológico de España 1:50.000 (2ª serie), Instituto Geológico y Minero de España, Madrid, Hoja 213, Pont de Suert, 1997.

875 Gartrell, A., Hudson, C., and Evans, B.: The influence of basement faults during extension and oblique inversion of the Makassar Straits rift system: Insights from analog models, Am Assoc Pet Geol Bull, 89, 495–506, https://doi.org/10.1306/12010404018, 2005.

Gasanzade, F., Pfeiffer, W. T., Witte, F., Tuschy, I., and Bauer, S.: Subsurface renewable energy storage capacity for hydrogen, methane and compressed air – A performance assessment study from the North German Basin, Renewable and Sustainable
880 Energy Reviews, 149, 111422, https://doi.org/10.1016/J.RSER.2021.111422, 2021.

Gawthorpe, R. L. and Hurst, J. M.: Transfer zones in extensional basins: their structural style and influence on drainage development and stratigraphy, Journal - Geological Society (London), 150, 1137–1152, https://doi.org/10.1144/gsjgs.150.6.1137, 1993.

Gibbs, A. D.: Structural evolution of extensional basin margins, J Geol Soc London, 141, 609–620,
885 https://doi.org/10.1144/gsjgs.141.4.0609, 1984.

Granado, P., Ferrer, O., Muñoz, J. A., Thöny, W., and Strauss, P.: Basin inversion in tectonic wedges: Insights from analogue modelling and the Alpine-Carpathian fold-and-thrust belt, Tectonophysics, 703–704, 50–68, https://doi.org/10.1016/j.tecto.2017.02.022, 2017.

Granado, P., Roca, E., Strauss, P., Pelz, K., and Muñoz, J. A.: Structural styles in fold-and-thrust belts involving early salt
890 structures: The Northern Calcareous Alps (Austria), Geology, 47, https://doi.org/10.1130/G45281.1, 2019.

Granado, P., Ruh, J. B., Santolaria, P., Strauss, P., and Muñoz, J. A.: Stretching and Contraction of Extensional Basins With Pre-Rift Salt: A Numerical Modeling Approach, Front Earth Sci (Lausanne), 9, https://doi.org/10.3389/feart.2021.648937, 2021.

Graveleau, F., Malavieille, J., Dominguez, S.: Experimental modeling of orogenic wedges: a review, Tectonophysics, 538, 1-66, 2012.

Hansen, T. H., Clausen, O. R., and Andresen, K. J.: Thick-and thin-skinned basin inversion in the Danish Central Graben, North Sea-the role of deep evaporites and basement kinematics, Solid Earth, 12, 1719–1747, https://doi.org/10.5194/se-12-1719-2021, 2021.

Kehle, R. O.: The Origin of Salt Structures, in: Evaporites and Hydrocarbons, edited by: Schreiber, B. C., Columbia University Press, New York Chichester, West Sussex, 345–404, https://doi.org/https://doi.org/10.7312/schr91060-008, 1988.

Konstantinovskaya, E. A., Harris, L. B., Poulin, J., and Ivanov, G. M.: Transfer zones and fault reactivation in inverted rift basins: Insights from physical modelling, Tectonophysics, 441, 1–26, https://doi.org/10.1016/j.tecto.2007.06.002, 2007.

Koopman, A., Speksnijder, A., and Horsfield, W. T.: Sandbox model studies of inversion tectonics, Tectonophysics, 137, https://doi.org/10.1016/0040-1951(87)90329-5, 1987.

Koyi, H., Jenyon, M. K., and Petersen, K.: The effect of basement faulting on diapirism, Journal of Petroleum Geology, 16, 285–312, https://doi.org/10.1111/j.1747-5457.1993.tb00339.x, 1993.

Lescoutre, R., Tugend, J., Brune, S., Masini, E., and Manatschal, G.: Thermal Evolution of Asymmetric Hyperextended Magma-Poor Rift Systems: Results From Numerical Modeling and Pyrenean Field Observations, Geochemistry, Geophysics, Geosystems, 20, https://doi.org/10.1029/2019GC008600, 2019.

Lohrmann, J., Kukowski, N., Adam, J., and Oncken, O.: The impact of analogue material properties on the geometry, kinematics, and dynamics of convergent sand wedges, J Struct Geol, 25, 1691–1711, https://doi.org/10.1016/S0191-8141(03)00005-1, 2003.

Martin-Roberts, E., Scott, V., Flude, S., Johnson, G., Haszeldine, R. S., and Gilfillan, S.: Carbon capture and storage at the end of a lost decade, One Earth, 4, 1569–1584, https://doi.org/10.1016/j.oneear.2021.10.002, 2021.

McClay, K. R.: Analogue models of inversion tectonics, Geol Soc Spec Publ, 44, https://doi.org/10.1144/GSL.SP.1989.044.01.04, 1989.

McClay, K. R.: The geometries and kinematics of inverted fault systems: A review of analogue model studies, Geol Soc Spec Publ, 88, https://doi.org/10.1144/GSL.SP.1995.088.01.07, 1995.

McClay, K. R.: Recent advances in analogue modelling: Uses in section interpretation and validation, Geol Soc Spec Publ, 99, https://doi.org/10.1144/GSL.SP.1996.099.01.16, 1996.

McClay, K. R., Dooley, T., Whitehouse, P., and Mills, M.: 4-D evolution of rift systems: Insights from scaled physical models, Am Assoc Pet Geol Bull, 86, 935–959, https://doi.org/10.1306/61eedbf2-173e-11d7-8645000102c1865d, 2002.

Mencós, J., Carrera, N., and Muñoz, J. A.: Influence of rift basin geometry on the subsequent postrift sedimentation and basin inversion: The Organyà Basin and the Bóixols thrust sheet (south central Pyrenees), Tectonics, 34, 1452–1474, https://doi.org/10.1002/2014TC003692, 2015.

Miocic, J. M., Alcalde, J., Heinemann, N., Marzan, I., and Hangx, S.: Toward Energy-Independence and Net-Zero: The Inevitability of Subsurface Storage in Europe, ACS Energy Lett, 7, 2486–2489, https://doi.org/10.1021/ACSENERGYLETT.2C01303/ASSET/IMAGES/LARGE/NZ2C01303_0001.JPEG, 2022.

Miró, J.; Ferrer, O.; Muñoz, J.A. and Manastchal, G.: Role of inheritance during tectonic inversion of a rift system in a thick-to thin-skin transition: Analogue modelling and application to the Pyrenean – Biscay System. Solid Earth, submitted.

Moragas, M., Vergés, J., Nalpas, T., Saura, E., Martín-Martín, J. D., Messager, G., and Hunt, D. W.: The impact of syn- and post-extension prograding sedimentation on the development of salt-related rift basins and their inversion: Clues from analogue modelling, Marine and Petroleum Geology, 88 (Supplement C), 985-1003, https://doi.org/10.1016/j.marpetgeo.2017.10.001, 2017.

935 Moragas, M., Vergés, J., Saura, E., Martín-Martín, J. D., Messager, G., Merino-Tomé, Ó., Suárez-Ruiz, I., Razin, P., Grélaud, C., Malaval, M., Joussiaume, R., and Hunt, D. W.: Jurassic rifting to post-rift subsidence analysis in the Central High Atlas and its relation to salt diapirism, Basin Research, 30, https://doi.org/10.1111/bre.12223, 2018.

Morley, C. K., Nelson, R. A., Patton, T. L., and Munn, S. G.: Transfer Zones in the East African Rift System and Their Relevance Hydrocarbon Eploration Rifts, The American Association of Petroleum Geologists Bulletin, 74, 1234–1253, 1990.

940 Mugnier, J.L., Baby, P., Coletta, B., Vinour, P., Bale, P., Leturmy, P.: Thrust geometry controlled by erosion and sedimentation: A view from analogue models, Geology, 25, 427-430, 1997.

Muñoz, J.A.: Evolution of a continental collision belt: ECORS-Pyrenees crustal balanced cross-section. In: McClay, K.R. (ed.). Thrust Tectonics. London, Chapman and Hall, 235-246, 1992.

Muñoz, J. A., Mencos, J., Roca, E., Carrera, N., Gratacós, O., Ferrer, O., and Fernández, O.: The structure of the South-Central-
945 Pyrenean fold and thrust belt as constrained by subsurface data, Geologica Acta, 16, 439–460, https://doi.org/10.1344/GeologicaActa2018.16.4.7, 2018.

Panien, M., Schreurs, G., and Pfiffner, A.: Sandbox experiments on basin inversion: testing the influence of basin orientation and basin fill, J Struct Geol, 27, 433–445, https://doi.org/10.1016/J.JSG.2004.11.001, 2005.

Peacock, D.C.P., and Sanderson, D.J.: Displacements, segment linkage and relay ramps in normal fault zones, Journal of
950 Structural Geology, 13 (6), 721-733,

Pinheiro, L. M., Wilson, R. C. L., Pena dos Reis, R., Whitmarsh, R. B., and Ribeiro, A.: The western Iberia Margin: a geophysical and geological overview, in: Proceedings of the Ocean Drilling Program, Scientific Results, vol. 149, edited by: Whitmarsh, R. B., Sawyer, D. S., Klaus, A., and Masson, D. G., Ocean Drilling Program, 1–23, https://doi.org/10.2973/odp.proc.sr.149.246.1996, 1996.

955 Ramos, A., Lopez-Mir, B., Wilson, E.P., Granado, P., Muñoz, J.A.: 3D reconstruction of syn-tectonic strata in a salt-related orogen: learnings from the Llert syncline (South-central Pyrenees), Geologica Acta, 18, 1-19, 2020

Rasmussen, E. S., Lomholt, S., Andersen, C., and Vejbæk, O. v.: Aspects of the structural evolution of the Lusitanian Basin in Portugal and the shelf and slope area offshore Portugal, Tectonophysics, 300, 199–225, https://doi.org/10.1016/S0040-1951(98)00241-8, 1998.

960 Ribeiro, A., Kullberg, M. C., Kullberg, J. C., Manuppella, G., and Phipps, S.: A review of Alpine tectonics in Portugal: Foreland detachment in basement and cover rocks, Tectonophysics, 184, 357–366, https://doi.org/10.1016/0040-1951(90)90448-H, 1990.

Richardson, N. J., Underhill, J. R., and Lewis, G.: The role of evaporite mobility in modifying subsidence patterns during normal fault growth and linkage, Halten Terrace, Mid-Norway, Basin Research, 17, 203–223, https://doi.org/10.1111/j.1365-
965 2117.2005.00250.x, 2005.

Robador, A., and Zamorano, M.: Mapa geológico de España 1:50.000 (2ª serie), Hoja 212, Campo, Instituto Geológico y Minero de España, Madrid, 1999.

Roma, M., Ferrer, O., Roca, E., Pla, O., Escosa, F. O., and Butillé, M.: Formation and inversion of salt-detached ramp-syncline basins. Results from analog modeling and application to the Columbrets Basin (Western Mediterranean), Tectonophysics, 745, 214–228, https://doi.org/10.1016/J.TECTO.2018.08.012, 2018a.

Roma, M., Vidal-Royo, O., McClay, K., Ferrer, O., and Muñoz, J. A.: Tectonic inversion of salt-detached ramp-syncline basins as illustrated by analog modeling and kinematic restoration, Interpretation, 6, T127–T144, https://doi.org/10.1190/INT-2017-0073.1, 2018b.

Roma, M., Ferrer, O., McClay, K. R., Muñoz, J. A., Roca, E., Gratacós, O., and Cabello, P.: Weld kinematics of syn-rift salt during basement-involved extension and subsequent inversion: Results from analog models, Geologica Acta, 16, https://doi.org/10.1344/GeologicaActa2018.16.4.4, 2018c.

Saïd, A., Baby, P., Chardon, D., and Ouali, J.: Structure, paleogeographic inheritance, and deformation history of the Southern Atlas foreland fold and thrust belt of Tunisia, Tectonics, 30, https://doi.org/10.1029/2011TC002862, 2011.

Sala, P., Pfiffner, O. A., and Frehner, M.: The Alpstein in three dimensions: fold-and-thrust belt visualization in the Helvetic zone, eastern Switzerland, Swiss J Geosci, 107, https://doi.org/10.1007/s00015-014-0168-6, 2014.

Santolaria, P., Granado, P., Carrera, N., Schneider, C. L., Ferrer, O., Snidero, M., Strauss, P., Pelz, K., Roca, E., and Muñoz, J. A.: From downbuilding to contractional reactivation of salt-sediment systems: Insights from analog modeling, Tectonophysics, 819, https://doi.org/10.1016/j.tecto.2021.229078, 2021a.

Santolaria, P., Ferrer, O., Rowan, M. G., Snidero, M., Carrera, N., Granado, P., Muñoz, J. A., Roca, E., Schneider, C. L., Piña, A., and Zamora, G.: Influence of preexisting salt diapirs during thrust wedge evolution and secondary welding: Insights from analog modeling, J Struct Geol, 149, https://doi.org/10.1016/j.jsg.2021.104374, 2021b.

Santolaria, P., Granado, P., Wilson, E.P., de Matteis, M., Ferrer, O., M., Strauss, P., Pelz, K., König, M., Oteleanu, A.E., Roca, E., Muñoz, J.A.: From salt-bearing rifted margins to fold-and-thrust belts. Insights from analogue modelling and Northern Calcareous Alps case study, Tectonics, 2022.

Schellart, W. P.: Shear test results for cohesion and friction coefficients for different granular materials: Scaling implications for their usage in analogue modelling, Tectonophysics, 324, https://doi.org/10.1016/S0040-1951(00)00111-6, 2000.

Schreurs, G., Buiter, S. J. H., Boutelier, D., Corti, G., Costa, E., Cruden, A. R., Daniel, J. M., Hoth, S., Koyi, H. A., Kukowski, N., Lohrmann, J., Ravaglia, A., Schlische, R. W., Withjack, M. O., Yamada, Y., Cavozzi, C., del Ventisette, C., Elder Brady, J. A., Hoffmann-Rothe, A., Mengus, J. M., Montanari, D., and Nilforoushan, F.: Analogue benchmarks of shortening and extension experiments, Geol Soc Spec Publ, 253, https://doi.org/10.1144/GSL.SP.2006.253.01.01, 2006.

Snidero, M., Muñoz, J.A., Carrera, N., Butillé, M., Mencos, J., Motamedi, H., Piryaei, A., Sàbat, F.: Temporal evolution of the Darmadan salt diapir, eastern Fars region, Iran, Tectonophysics 766, 115-130, https://doi.org/10.1016/j.tecto.2019.06.006.

Sommaruga, A.: Décollement tectonics in the Jura foreland fold-and-thrust belt. Marine and Petroleum Geology,16, 111–134, 1999.

Soto, J.I., Finch, J., Tari, G.: Permo-Triassic Salt Provinces of Europe, North Africa and the Atlantic Margins. Tectonics and Hydrocarbon Potential. Elsevier, 608pp, 2017.

Stapel, G., Cloetingh, S., and Pronk, B.: Quantitative subsidence analysis of the Mesozoic evolution of the Lusitanian basin (western Iberian margin), Tectonophysics, 266, 493–507, https://doi.org/10.1016/S0040-1951(96)00203-X, 1996.

Stewart, S. A. and Coward, M. P.: Synthesis of salt tectonics in the southern North Sea, UK, Mar Pet Geol, 12, 457–475, https://doi.org/10.1016/0264-8172(95)91502-G, 1995.

Stewart, S. A., Harvey, M. J., Otto, S. C., and Weston, P. J.: Influence of salt on fault geometry: Examples from the UK salt basins, Geol Soc Spec Publ, 100, 175–202, https://doi.org/10.1144/GSL.SP.1996.100.01.12, 1996.

Stewart, S. A., Ruffell, A. H., and Harvey, M. J.: Relationship between basement-linked and gravity-driven fault systems in the UKCS salt basins, Mar Pet Geol, 14, 581–604, https://doi.org/10.1016/S0264-8172(97)00008-1, 1997.

Stewart, S. A.: Salt tectonics in the North Sea Basin: A structural style template for seismic interpreters, Geol Soc Spec Publ, 272, 361–396, https://doi.org/10.1144/GSL.SP.2007.272.01.19, 2007.

Storti, F., and McClay, K.R.: Influence of syntectonic sedimentation on thrust wedges in analogue models, Geology, 23, 999–1002, 1995.

Strauss, P., Granado, P., and Muñoz, J. A.: Subsidence analysis of salt tectonics-driven carbonate minibasins (Northern Calcareous Alps, Austria), Basin Research, 33, 968–990, https://doi.org/10.1111/BRE.12500, 2021.

Tavani, S., Bertok, C., Granado, P., Piana, F., Salas, R., Vigna, B., and Muñoz, J. A.: The Iberia-Eurasia plate boundary east of the Pyrenees, Earth Sci Rev, 187, 314–337, https://doi.org/10.1016/j.earscirev.2018.10.008, 2018.

Tavani, S. and Granado, P.: Along-strike evolution of folding, stretching and breaching of post-salt strata in the Plataforma Burgalesa extensional forced fold system (northern Spain). Basin Res, 27: 573-585. https://doi.org/10.1111/bre.12089, 2015.

Tugend, J., Manatschal, G., Kusznir, N. J., Masini, E., Mohn, G., and Thinon, I.: Formation and deformation of hyperextended rift systems: Insights from rift domain mapping in the Bay of Biscay-Pyrenees, Tectonics, 33, 1239–1276, https://doi.org/10.1002/2014TC003529, 2014.

Velaj, T., Davison, I., Serjani, A., Alsop, I.: Thrust tectonic and the role of evaporites in the Ionian zone of the Albanides. AAPG Bull 83(9):1408–1425, 1999.

Vendeville, B. C., Hongxing Ge, and Jackson, M. P. A.: Scale models of salt tectonics during basement-involved extension, Petroleum Geoscience, 1, 179–183, https://doi.org/10.1144/petgeo.1.2.179, 1995.

Weijermars, R. and Schmeling, H.: Scaling of Newtonian and non-Newtonian fluid dynamics without inertia for quantitative modelling of rock flow due to gravity (including the concept of rheological similarity), Physics of the Earth and Planetary Interiors, 43, https://doi.org/10.1016/0031-9201(86)90021-X, 1986.

White, N. J., Jackson, J. A., and McKenzie, D. P.: The relationship between the geometry of normal faults and that of the sedimentary layers in their hanging walls, J Struct Geol, 8, 897–909, https://doi.org/10.1016/0191-8141(86)90035-0, 1986.

Withjack, M. O. and Callaway, S.: Active normal faulting beneath a salt layer: An experimental study of deformation patterns in the cover sequence, Am Assoc Pet Geol Bull, 84, 627–651, https://doi.org/10.1306/c9ebce73-1735-11d7-8645000102c1865d, 2000.

Withjack, M. O., Olson, J., and Peterson, E.: Experimental Models of Extensional Forced Folds, Am Assoc Pet Geol Bull, 74, 1038–1054, https://doi.org/10.1306/0C9B23FD-1710-11D7-8645000102C1865D, 1990.

Ziegler, P. A. and van Hoorn, B.: Evolution of North Sea Rift System, Extensional tectonics and stratigraphy of the North Atlantic margins, 471–500, https://doi.org/10.1306/M46497C31, 1989.

Zwaan, F., Schreurs, G., Buiter, S., Ferrer, O., Reitano, R., Rudolf, M., and Willingshofer, E.: Analogue modelling of basin inversion: a review and future perspectives, Solid Earth Discussions [preprint], https://doi.org/https://doi.org/10.5194/se-2022-8, 2022.